SKELETAL MUSCLE DEFORMATION ANALYSIS USING DIFFUSION TENSOR MAGNETIC RESONANCE IMAGING

by

Pinar Akyazi

B.S., Electrical and Electronics Engineering, Bogazici University, 2010

Submitted to the Institute for Graduate Studies in
Science and Engineering in partial fulfillment of
the requirements for the degree of
Master of Science

Graduate Program in Electrical and Electronic Engineering

Boğaziçi University

2013

SKELETAL MUSCLE DEFORMATION ANALYSIS USING DIFFUSION TENSOR MAGNETIC RESONANCE IMAGING

APPROVED BY:

Assoc. Prof. Burak Acar (Thesis Supervisor)	.....
Assoc. Prof. A. Can Yücesoy (Thesis Co-supervisor)	.....
Prof. Emin Anarım	.....
Assist. Prof. Ali Emre Pusane	.....
Assoc. Prof. Mehmet Burçin Ünlü	.....

DATE OF APPROVAL: 02.08.2013

ACKNOWLEDGEMENTS

First I would like to thank my supervisor, Assoc. Prof. Burak Acar, not only for his guidance but also for his belief and patience for he has taught me valuable life lessons throughout the whole time we worked together.

I would like to thank my co-supervisor Assoc. Prof. A. Can Yücesoy for his support and motivation, and for always managing to point out the best in everything, and the members of my evaluation committee for their sincerty and encouragement at every encounter.

I would like to give my special thanks to Prof. Bülent Sankur and Prof. Kadri Özçaldıran. Without their support throughout all these years, I would not be the person I am today.

I should not forget to thank my colleagues Uluç Pamuk and Arda Arpak for their share in my work and efforts. Also I am thankful that I have had the chance to share my working hours with Neda Marvasti, Serkan Çimen and Abdülkadir Yazıcı, for the joy they have brought every time I struggled.

Special thanks to my family, Magic and Melih, for their unconditional love and support through good times and bad, and my dear friend Burçin for being there no matter what and for reminding me of who I am.

I am especially grateful to Assoc. Prof. Murat Saraçlar for he has been beside me at each and every step of the way in every way possible, for believing in me and making me believe in myself.

This thesis was supported by grants from TUBITAK project (111E084).

ABSTRACT

SKELETAL MUSCLE DEFORMATION ANALYSIS USING DIFFUSION TENSOR MAGNETIC RESONANCE IMAGING

Skeletal muscles are highly organized tissues formed of fiber bundles packed together. Muscle fibers have distinct orientations which makes them a favorable subject for diffusion tensor imaging (DTI) based analyses. DTI provides *in vivo* measures revealing the structural characteristics of tissues based on diffusion anisotropies of water molecules within structures. Local fiber orientations can be extracted for deformation analysis of the spatial distribution of diffusion and strain characteristics along fiber directions. This work aims to present a framework for the assessment of local strain and diffusion anisotropy changes as skeletal muscles of human subjects (n=3) become deformed by moving from a flexed configuration (150° knee angle) to an extended configuration (180° knee angle). Changes between the diffusion anisotropy indices and strain coefficients along fiber tracts between the tibialis anterior muscle ends are computed, visualized and modeled to account for heterogeneous changes in the microstructure resulting from deformation. Results are indicators of effects of myofascial force transmission on human muscles in vivo, including local differences between sarcomere length changes (maximal lengthening and shortening equals 34.62% and -33.78%, respectively) and diffusivity changes in the proximo-distal direction as well as in the transverse plane. The demonstrated methodology also provides an image processing toolbox for the thorough analysis of skeletal muscles. Final results presented here can have clinical implications by contributing to explaining and improving the treatment options of movement limitations.

ÖZET

İSKELET KASLARINDA DİFÜZYON TENSÖR MANYETİK REZONANS GÖRÜNTÜLERİ İLE DEFORMASYON ANALİZİ

İskelet kasları lif demetlerinin bir araya gelmesiyle oluşmuş, yüksek derecede düzenli yapıya sahip dokulardır. Kas liflerinin belli doğrultuda dizilmiş olmaları, difüzyon tensör görüntülemesi (DTG) üzerinden yapılabilecek analizlere uygun fizyolojinin varlığına işaret eder. DTG, yaşayan organizmada dokuların yapısal özelliklerini su moleküllerinin doku içindeki difüzyon eşyönsüzlüğüne ilişkin ölçümlerle ortaya çıkarır. Yerel lif yönelimleri kullanılarak difüzyon ve gerilim özelliklerinin uzamsal dağılımının fiber yönünde deformasyon analizi sağlanır. Bu tez, insan iskelet kaslarının kısa ve gergin (diz açısı sırayla 150° ve 180°) pozisyonları arasındaki deformasyon sonucu oluşan yerel difüzyon eşyönsüzlüğü ve gerilim değişimlerine ilişkin bir model oluşturmayı amaçlar. Analiz için alt bacakta kaval kemiği kası lifleri seçilerek, kas uzunluğu boyunca difüzyon eşyönsüzlüğü indisleri ve gerilim katsayıları hesaplanır, görselleştirilir ve iç yapıdaki heterojenlikleri ortaya çıkarmak amacıyla modellenir. Sonuçlar, miyofasiyal kuvvet iletiminin varlığını alt bacaktan yukarıya ve transvers düzlem üzerinde sarkomer uzunlukları (3 denek için maksimum %33.78 kısalma ve %34.62 uzama) ve difüzyon dağılımındaki yerel değişimler ile kanıtlar. Uygulanan yöntemler ile iskelet kaslarının özelliklerini analiz edebilmeye yarayan bir imge işleme yazılımı oluşturulmuştur. Sunulan sonuçların hareket kabiliyetinde azalmanın nedenlerine ve tedavi yöntemlerine ilişkin önemli klinik çıkarımlara katkıda bulunması beklenmektedir.

TABLE OF CONTENTS

LIST OF FIGURES

LIST OF TABLES

LIST OF SYMBOLS

A	Signal attenuation
$\mathbf{D}$	Arbitrary diffusion tensor
$\overline{\mathbf{D}}$	Interpolated diffusion tensor
D	Diffusion coefficient
$\mathbf{E}$	Arbitrary strain tensor
$\overline{\mathbf{E}}$	Interpolated strain tensor
$\mathbf{F}$	Deformation gradient tensor
N_{EX}	Number of excitations
m	Parameter average over all fibers
s	Parameter standard deviation over all fibers
T	Mapping of MRI datasets
T^*	Mapping of DTI datasets
$\vec{t}$	Tract direction at a given voxel
$\mathbf{u}$	Displacement vector field in material coordinates
$\vec{u_N}$	Eigenvector of the strain tensor associated with the tensor's negative eigenvalue of largest absolute magnitude
$\vec{u_P}$	Eigenvector of the strain tensor associated with the tensor's positive eigenvalue
$\vec{v_i}$	i^{th} eigenvector of the diffusion tensor
w_i	Weight assigned to the $i^{th} neighbor voxel$
Δ	Difference between deformed and base configurations
ε_N	Negative eigenvalue of largest absolute value of the strain tensor
ε_P	Positive eigenvalue of the strain tensor
θ	Muscle pennation angle
λ_i	i^{th} eigenvalue of the diffusion tensor
$\mathcal{N}(\mu, s)$	Gaussian distribution with mean μ and standard deviation σ
ρ	Muscle density in g/mm^3

ψ_b	MRI to DTI transformation in base configuration
ψ_d	MRI to DTI transformation in deformed configuration
∇u	Material displacement gradient tensor

LIST OF ABBREVIATIONS

3D	Three dimensional
ADC	Apparent diffusion coefficient
DAI	Diffusion anisotropy index
DTI	Diffusion tensor imaging
DT-MRI	Diffusion tensor magnetic resonance imaging
DWI	Diffusion weighted image
EDL	Extensor digitorum longus
EHL	Extensor hallucis longus
EPI	Echo-planar imaging
ext	Extended configuration of the leg
FA	Fractional anisotropy
FEM	Finite element method
FOV	Field of view
flx	Flexed configuration of the leg
GL	Gastrocnemius lateral
GM	Gastrocnemius medial
LDC	Linear diffusion coefficient
MD	Mean diffusivity
MVC	Maximum voluntary contraction
NMR	Nuclear magnetic resonance
PCSA	Physical cross-sectional area
PDD	Principal diffusion direction
ROI	Region of interest
SC	Strain coefficient
SNR	Signal-to-noise ratio
SOL	Soleus
TA	Tibialis anterior
TR	Repetition time
TE	Echo time

1. INTRODUCTION

Diffusion tensor magnetic resonance imaging (DT-MRI or DTI) provides statistical and physiological measures related to bodily structures, based on the random Brownian motion, or diffusion, of water molecules. It is an *in-vivo* technique which maps the diffusion of water molecules to reveal the microstructural architecture. Within organized fibrous tissue such as brain white matter, cardiac and skeletal muscles, water diffuses anisotropically where the diffusion rate is faster along the microstructural orientation. Principal diffusion direction (PDD) based tractography algorithms reconstruct the tissue fibers and provide a frame of reference for further analysis along the tracts.

Movement of the limbs between different positions occur because of the contractions and lengthening of skeletal muscles. When a muscle undergoes any of the two states, the overall cross sectional area and length of the muscle are altered whereas muscle volume remains constant. The alterations occur in all levels within the muscle complex; fiber bundles and individual fibers, i.e. muscle cells comprised of sarcomeres arranged in series. Muscle contraction or relaxation simultaneously occurs with force transmission and results in a deformation of the microstructure. The nature of force transmission affects the deformation characteristics. From the classical perspective, myotendinous junctions are widely accepted as the exclusive sites for force transmission. This point of view has intramuscular and epimuscular implications on the understanding of muscular mechanics. From the intramuscular aspect, muscle fibers are regarded as independently functioning units because mechanical connections between the muscle fibers and the extracellular matrix are considered to exist only at fiber ends [1]. Therefore in classical muscle mechanics, muscle force was measured by fully dissecting the target muscle except for its innervention and blood supply, and only at one tendon exclusively. This approach predicates that the muscle studied *in situ* is fully isolated from its surroundings and the muscle force exerted at the tendon from which the measurements are taken is equal to the force exerted at the other tendon [1]. *Ex-vivo* measurements performed on isolated muscles suggested that muscles are independent units from their surroundings and that the length-force characteristics of a muscle is unique to that muscle. However, intramuscular connective tissue stroma and muscle fibers are connected to each other along fibers and it was shown that muscular force is

transmitted within endomysial tunnels [2–4]. In addition to this intramuscular myofascial force transmission, epimuscular myofascial force transmission occurs within direct and indirect intermuscular connections such as collagenous linkages between adjacent fibers and neurovascular tracts, respectively, as well as extramuscular connections binding muscular and non-muscular tissues [1,5]. Research concentrated on *in vivo* experiments show that, contrary to the classical idealizations, myofascial force transmission affects the length-force characteristics of the muscle by introducing proximo-distal force differences and heterogeneities in the distribution of strain, i.e. relative lengthening or shortening, along sarcomeres in series and in parallel. Therefore muscle relative position is said to play a major role in depicting the length-force characteristics, which in turn means that these characteristics are not fixed properties of muscles [6,7].

Recent findings have shown that local strains within muscles are much higher than global strains imposed on them [8], which indicates the presence of epimuscular myofascial force transmission contrary to the classical point of view. Modeling skeletal muscles in two distinct domains (intracellular domain and extracellular matrix domain) using finite element method (FEM) by elastically linking the respective meshes to account for the trans-sarcolemmal attachments of the muscle fibers cytoskeleton and extracellular matrix (i.e. linked fiber-matrix mesh model), the interaction between these domains and the significance of myofascial force transmission can be investigated. It was shown that any missing link within the trans-sarcolemmal connections or inadequate linking to the extracellular matrix result in deformed myofibers due to the lacking of mechanical support and impairment of a pathway of force transmission by the extracellular matrix, which in turn leads to a drop in muscle force. Furthermore, the force drop becomes more dramatic if the impairment is located more towards the center of the muscle model. Manipulating the linking stiffness at selected locations within the modeled muscle resulted in varying local strains along muscle fibers as a consequence of the interactions between fibers and the extracellular matrix [4]. In addition, mean sarcomere lengths were distributed heterogeneously within individual fibers. Therefore both serial and parallel sarcomere length heterogeneities are present within skeletal muscles. These discoveries have major clinical implications in the sense that conventional surgical techniques may have to be revised and improved considering the findings. Because of the epimuscular connections, clinical dissection of target muscles interfere with myofascial force transmission and the remaining connections can still transmit muscle force to a high extent [6]. Surgeries to restore muscle function have to be per-

formed while taking into account these newly introduced pathways, and that muscles are not independent neither from their synergists nor muscular or non-muscular surroundings. Both the mechanical mechanism of clinical interventions and the adaptation mechanisms after surgery are affected by epimuscular myofascial force transmission [9]. Aponeurotomy, for instance, which is the dissection of flat intramuscular tendon layers, was considered as an intramuscular intervention to lengthen the muscle and/or reduce the muscle force, but now extramuscular connections have to be taken into consideration as well if limited joint range of motion is to be corrected [6, 10–12]. Moreover, it is possible to relate the causes of movement limitations due to changes in extramuscular tissue microstructure, such as spastic paresis, with the epimuscular myofascial force transmission. Experiments performed on human spastic Gracilis muscle prove that if activated alone, spastic muscle shows no abnormal mechanics representative of joint movement disorder. On the other hand, simultaneous stimulation of other muscles as in daily activities may change this situation [13]. Consideration of these indications and impacts of epimuscular myofascial force transmission can improve the understanding and treatment options of such conditions.

Studies on skeletal muscles using fiber tractography have revealed the diffusion characteristics of fibers on specific local positions and the results have been presented using global averages [14–16]. Studies involving DTI and strain measurements together have compared the diffusion and strain distributions of skeletal muscles by means of analyzing the respective tensor characteristics within local boundaries [7]. However, the assessment of global and local strains using MRI techniques has not been performed along the direction of muscle fibers, which is the physiologically important variable.

The aim of this study, from the biomechanical regard, is to assess the deformation in skeletal muscles by measuring the spatial distribution of local and global strains along the direction of muscle fibers. DT-MRI data is used not only to construct the fiber tracts for strain analysis but also to provide diffusion related measures revealing the changes in the spatial distribution of diffusion characteristics along skeletal muscle fibers as a result of any deformation. The goal of this work from the engineering regard includes building an image processing toolbox for the analysis of skeletal muscle architecture. The combined diffusion and strain analyses can lead to a better understanding of biomechanical properties of skeletal

muscles and thus improve clinical applications and treatment of movement limitations.

This thesis is organized as follows: Chapter 2 provides the background information on DT-MRI and the anatomy of skeletal muscles, followed by a review of previous studies involving DT-MRI of skeletal muscles and the assessment of muscular force transmission. Chapter 3 describes the methodology and tools used for the experiments. Results are delivered in Chapter 4. Discussion of the results are presented in Chapter 5, with the concluding remarks stated in Chapter 6.

2. BACKGROUND

DTI involves noncollinearly directed diffusion weighted image (DWI) measurements in at least six directions, where the pulse sequence is designed to be sensitive to the directionality of diffusion [15,17]. DTI studies have been used to reveal microstructural characteristics of various parts of the body, including the brain, cardiac muscles, kidney and skeletal muscles, where diffusion tensors have been shown to represent cell geometry [18]. Especially in fibrous tissues for which cellular fibers elongate in a dominant direction, the diffusion of water molecules is highly anisotropic and this directionality can be detected from the eigen-analysis of the diffusion tensor. Water molecules tend to diffuse readily along the principal fiber axis which conforms with the principal eigenvector [18–20].

2.1. Diffusion Tensor Magnetic Resonance Imaging

Diffusion tensor magnetic resonance imaging emerged as a new nuclear magnetic resonance (NMR) imaging technique, in which each voxel comprises an effective diffusion tensor [21]. Plain diffusion MRI uses a single scalar apparent diffusion coefficient at each voxel from a series of diffusion weighted images (DWIs) [22]. However, in case of molecular displacements in multiple directions, or in other words, anisotropy, diffusion MRI measurements become inadequate as diffusion can no longer be characterized in a scalar setting. Instead, a three dimensional tensor $\mathbf{D}$ is required to describe the molecular mobility along each direction and correlation between these directions [23]:

$$\mathbf{D} = \begin{bmatrix} D_{xx} & D_{xy} & D_{xz} \\ D_{yx} & D_{yy} & D_{yz} \\ D_{zx} & D_{zy} & D_{zz} \end{bmatrix} \tag{2.1}$$

The diffusion tensor is symmetric and positive semi-definite. To construct a full diffusion tensor, diffusion weighted images along at least six non collinear directions are therefore required. These images can be collected using diffusion sensitized MRI pulse sequences such

as echoplanar imaging (EPI) [23]. Also a non diffusion weighted image is needed for which the b-factor, or $b = 0$.

The effect of diffusion on the MRI signal is an attenuation A, which depends on D and on the b-factor, and can be expressed as follows in an isotropic medium:

$$A = exp(-bD) \tag{2.2}$$

The presence of anisotropy introduces the second-order tensor along with the symmetric second-order **b**-matrix instead of the scalar b-value and equation 2 along a single gradient direction becomes:

$$A = exp(-b_{xx}D_{xx} - b_{yy}D_{yy} - b_{zz}D_{zz} - 2b_{xy}D_{xy} - 2b_{xz}D_{xz} - 2b_{yz}D_{yz}) \tag{2.3}$$

Given the at least six attenuations obtained from DWI and $b = 0$ intensities along with the **b**-matrix at each voxel, the distinct elements of the diffusion tensor can be computed.

The diffusion tensor can be visualized as an ellipsoid where the three principal axes represent the eigenvectors of the tensor and the associated eigenvalues depict the relative diffusivity along each direction. In this setting, the key to DTI is that water readily diffuses along the direction associated with the greatest eigenvalue and this direction concurs with the orientation of highly organized tissue microstructure. Examples to such organizations are present within the brain white matter [19], cardiac muscles [24] and skeletal muscles [15, 25]. All of these structures are composed of fibrous tissue extending along a principal direction, within which a typical diffusion tensor would appear prolate rather than oblate, suggesting a microstructural orientation.

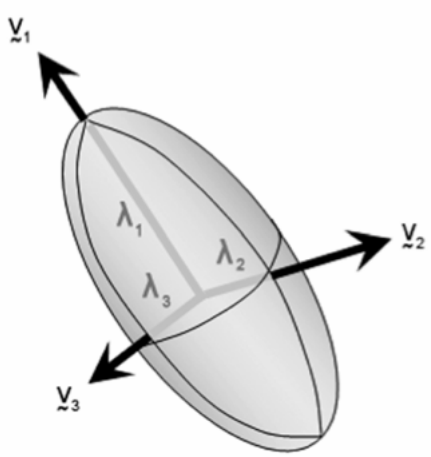

Figure 2.1. The diffusion ellipsoid characterized by the tensor eigenvectors and the associated eigenvalues [26].

The mathematical representation of the eigenanalysis of the diffusion tensor is:

$$\mathbf{D} = \begin{bmatrix} D_{xx} & D_{xy} & D_{xz} \\ D_{yx} & D_{yy} & D_{yz} \\ D_{zx} & D_{zy} & D_{zz} \end{bmatrix} = \begin{bmatrix} \vdots & \vdots & \vdots \\ \vec{v_1} & \vec{v_2} & \vec{v_3} \\ \vdots & \vdots & \vdots \end{bmatrix} \begin{bmatrix} \lambda_1 & 0 & 0 \\ 0 & \lambda_2 & 0 \\ 0 & 0 & \lambda_3 \end{bmatrix} \begin{bmatrix} \cdots & \vec{v_1} & \cdots \\ \cdots & \vec{v_2} & \cdots \\ \cdots & \vec{v_3} & \cdots \end{bmatrix} \tag{2.4}$$

where $\lambda_1 > \lambda_2 > \lambda_3$ are the eigenvalues of the tensor and $\vec{v_1}, \vec{v_2}$ and $\vec{v_3}$ are the associated eigenvectors. $\vec{v_1}$ is also referred as the principal diffusion direction.

DTI is an advantageous modality as it requires short acquisition time, provides information about diffusion orientation and anisotropy and examination is well tolerated by patients [27]. The information about the degree of anisotropy within the diffusion ellipsoid can be reduced into a single scalar for easier interpretation, referred as a diffusion anisotropy index (DAI). There are several proposed DAIs to measure and compare diffusion statistics. A basic DAI is the apparent diffusion coefficient (ADC) or mean diffusivity (MD), which accounts for the average diffusivity of a certain voxel, with the effects of anisotropy averaged out. Another common DAI called the fractional anisotropy (FA) is a relative measure specifying what fraction of the total diffusion described by **D** is anisotropic. FA index varies between 0 (isotropic

diffusion, i.e. $\lambda_1 = \lambda_2 = \lambda_3$) and 1 (completely anisotropic diffusion, i.e. $\lambda_1 \gg \lambda_2 = \lambda_3 = 0$).

$$FA = \sqrt{\frac{3}{2}} \frac{\sqrt{(\lambda_1 - \lambda_{av})^2 + (\lambda_2 - \lambda_{av})^2 + (\lambda_3 - \lambda_{av})^2}}{\sqrt{\lambda_1^2 + \lambda_2^2 + \lambda_3^2}} \tag{2.5}$$

$$ADC = \frac{\lambda_1 + \lambda_2 + \lambda_3}{3} \tag{2.6}$$

where λ_{av} refers to ADC itself. It must be noted that these DAI are rotationally invariant, i.e. they do not change when the tensor is rotated. Hence they can be calculated for any tensor orientation, without tensor diagonalization. As the invariants are independent of tissue orientation with respect to the static magnetic field, comparisons between different subjects are allowed [28].

The microstructural characteristics of organized soft fibrous tissue can be revealed by tracing the PDD along voxels. Fiber tract trajectories are formed from consecutive principal diffusion directions as PDD confirms with tissue orientation. Aside from the advantages, DTI has several drawbacks where complex fiber architecture is present, such as the crossing, branching and merging fibers within the brain white matter. Tractography results are vulnerable to severe artifacts such as noise, motion and eddy currents. In addition, DTI resolution cannot be reduced below the physical cross section of the fiber since lower voxel sizes cannot account for the confined diffusion characteristics within the organized tissue [19, 29]. The low signal-to-noise ratio (SNR) and resolution problems have been addressed with faster and more powerful gradients. Although DTI is a hypothesis based method and there are no gold standards for tractography results, proper acquisition schemes and enhanced tractography algorithms yield reliable fiber reconstruction from the images [30, 31].

2.2. Anatomy of Skeletal Muscles, Human Leg and Calf Muscle

Skeletal muscles possess a high degree of structural and functional organization, which helps them build up force, produce mechanical actions and shorten. This organization is also highly structurally anisotropic as the generation of mechanical events which have a direction

and magnitude requires such anisotropy.

Skeletal muscles are organized in muscle fiber units that are bundled together in packs of hundreds to thousands. These fibers are mostly cylindrical in shape with diameters between 20 and 70μm and have multiple nuclei. The fibers stacked on top of each other generally originate from stiffer structures, usually at proximal ends, and insert into more compliant and usually at distal ends. Each fiber consists of myofibrils, which are the contractile units containing regulatory, contractile and structural protein filaments. Interconnecting tubules surrounding the myofibrils make up the sarcoplasmic reticulum. All of these structures lay parallel to the longitudinal axis of the muscle fiber. The directional histology and morphology of skeletal muscles allow DTI measurements to reveal the characteristics of their architecture [32].

Human calf muscle is located at the back of the lower leg and contains the anterior crural department where the foot dorsiflexors are located. An axial cross section of the calf muscle contains tibialis anterior muscle (TA), soleus muscle (SOL) and the medial and lateral heads of the gastrocnemius muscle (GM and GL, respectively).

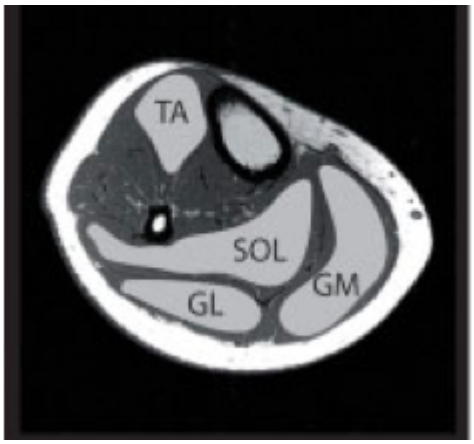

Figure 2.2. Axial cross section of the human calf muscle from a 31-year-old female subject [16].

Human TA muscle has a bipennate structure optimally designed for force production, where the fibers of TA insert into a central aponeurosis with an angle referred as the pennation angle, formed between the local tangent to the muscle fibers and the local tangent to the aponeurosis. TA fibers elongate along the sides of the aponeurosis on the vertical axis [15, 16].

2.3. Literature Review

2.3.1. DT-MRI of Skeletal Muscles

Studies about the biological, histological and morphological characteristics of skeletal muscles based on DTI are concentrated on fiber tractography and DAI measures along the computed tracts. It has been shown that *in vitro* and *in vivo* tracking of muscle fibers are feasible, and can be used to investigate muscle structure and function relationships. Unipennate and bipennate architecture of the calf muscle groups could be identified and fibers could be tracked from aponeurosis to aponeurosis. Fiber tracts of the TA muscle, for instance, show the bipennate insertion of the muscle fascicles on the distal aponeurosis and the unipennate arrangement at the more proximal location, which conforms to the known fiber organization of the muscle [15, 33].

Significant changes in diffusional characteristics in terms of FA and ADC were reported within the human calf muscle by passive shortening and stretching. An increased mean diffusivity in the shortened muscle groups is revealed, physiologically coinciding with an increased cross-sectional area of the muscle fiber. From plantarflexion to dorsiflexion, the changes in FA and ADC were ascribed mainly to λ_2 and λ_3 whereas λ_1 showed no significant change, since λ_1 is independent of the muscle diameter. λ_2 and λ_3, on the other hand, represent the diffusivities along the directions perpendicular to the fiber orientation, and any increase or decrease in the fiber cross section would alter the diffusivity along the cross sectional direction proportional to the change. Shortening of the muscle fiber yields an increased cross section and a decreased length since during any activity muscle volume remains constant, and an increased cross section results in facilitated diffusion of water in radial directions. Stretching of the muscles caused elevated FA and decreased MD, on the contrary, passive shortening decreased FA and increased MD [16].

Many other measurements can help inferring tissue microstructure characteristics, such as comparing the eigenvalues with each other during passive flexion and extension of the ankle. Previous studies on cardiac muscles revealed that λ_1 corresponds to the fiber direction, λ_2 corresponds to the direction parallel to myocardial sheets, and λ_3 corresponds to the direction

that is normal to the sheets [34]. Experiments on the human calf muscle have analogously attributed λ_2 to the direction along sheets of muscle fibers within the endomysium (the region between fibers) and strong correlations between the physical cross-sectional area (PCSA) of the muscle and λ_3 were observed [35]. PCSA is an important measure regarding muscle architecture and is directly proportional to the maximum tetanic tension generated by the muscle. It theoretically corresponds to the sum of the cross sections of all fibers in a muscle, and can be expressed as:

$$PCSA = \frac{muscle\,mass \cdot \cos\alpha}{\rho \cdot fiber\,length} \tag{2.7}$$

where PCSA is given in mm^2, muscle mass is in grams and fiber length is in millimeters. ρ is the muscle density in g/mm^3 and α is the surface pennation angle [36]. PCSA and fiber length, with their proportionalities to muscle force and velocity, respectively, are the main two characteristics that govern the functional attributes of a muscle. The combination of a correlation between λ_3 and PCSA, along with FA and other statistics from the remaining eigenvalues help characterize diffusion properties of different muscle groups. In addition, measurements on the orientation angle between the main fiber axis and the vertical axis, and the angle in the axial plane between the main fiber axis and the horizontal axis reveal clear differences between muscle groups, depending on the anatomical shape of the musculature. DTI is therefore capable of distinguishing anatomically and functionally different muscles at the same region from each other.

DTI plays an important role in distinguishing healthy and injured tissues as well. It was proposed that an injury such as a muscle tear or hematoma in human skeletal muscle disrupts the microstructural integrity and therefore can be detected from the alterations in the measured diffusion statistics. Indeed, injured tissue diffusion tensor eigenvalues were found elevated compared to healthy controls. Similarly, ADC was increased whereas FA was decreased. The results correlate well with the theoretical assumption that injuries would disrupt the muscle cell membranes, increase water diffusion and hence reduce the anisotropic fraction of the total diffusion [37]. Another detailed analysis based on skeletal muscle ischemia-reperfusion injury shows DTI can be used to assess the induced damage. Ischemia-reperfusion damages cause edema, infiltration of inflammatory cells and a disruption in the normal muscle architecture.

For equivalents of 50 minutes and 4 hours of ischemic conditions and their following reperfusions in TA, ADC was increased during the ischemic period and decreased during reperfusion. On the contrary, FA was decreased during the ischemic period and increased during reperfusion. The duration and severity of ischemic stress affected the changes in the eigenvalues; for mild ischemia all eigenvalues decreased but the decrease in λ_2 and λ_3 were more dramatic compared to λ_3. In both cases all eigenvalues increased during reperfusion, with λ_3 showing the largest increase. Twenty four hours after the reperfusion damage, no correlation between λ_1 and histological damage in terms of interstitial fluid accumulation and infiltrates was detected, however, λ_2 and λ_3 were correlated with interstitial fluid accumulation and the percentages of damaged and round cells. λ_3 also correlated with the general damage score and the amount of infiltrates. This finding suggests that λ_2 and λ_3 have different structural significances [32, 37]. Another research suggests that λ_2 and λ_3 have distinct biological bases, based on the fact that induced muscle atrophy in rat sciatic nerve caused an increase in FA, decrease in λ_2 after 4 weeks and a decrease in λ_3 after 8 weeks, although no correlation between fiber diameter change and λ_2 and λ_3 was detected [38].

It is qualitatively and quantitatively shown that *in vivo* DT-MRI fiber tracking and direct anatomical inspection produce equivalent results in measuring the pennation angle (θ). Mechanical models of muscle function require knowledge of muscle architecture. Noninvasive *in vivo* imaging modalities rule out the limitations of *ex vivo* architecture measurements such as artifacts of fixation or unknown health conditions. Ultrasound measurements, as an example, allow real time assessment of fascicle length and pennation angle changes, however are restricted to one region and cannot cover regional variations in pennation within a single measurement [18]. In spite of the lower resolution, DTI rules out the mentioned disadvantages and allows the detection of within-muscle heterogeneity, simultaneous capturing of multiple members of a synergistic group of muscles, fiber length, pennation angle and PCSA measurements throughout a large volume of data [18].

Positioning a region of interest (ROI) on a single DT image provides cross sectional measurements of FA, ADC and other diffusion statistics. However, this method only covers a small volume of the muscle at a fixed level. Tractography, on the other hand, allows for the inspection of muscular microstructure within full fiber length by extracting the fibers through

a single ROI [39].

The arrangement of skeletal muscle fibers makes them an ideal subject of DTI based fiber tractography, because unlike the white matter tracts in the brain, skeletal muscle fibers do not kiss, cross or merge. Rather, they originate from and insert into specific aponeuroses, bones or fascia and are aligned parallel to each other within their unipennate, bipennate or multipennate structures. For example, TA runs from either the tibia or the superficial fascia of the anterior compartment to the central aponeurosis. Such knowledge of start and end points make it possible to carry out a quantitative assessment of fiber tracking. The accuracy of the tractography results are affected by intrinsic muscle properties, image acquisition and artifacts such as movement and noise, and the tractography algorithm itself. Again for the TA muscle, it is possible to design the algorithm to choose the tract seeds from a mesh definition of the central aponeurosis and set the proper stopping criterion essentially depending on length, curvature and FA threshold. The aponeurosis mesh can also be used as a mask defining the muscle boundaries. Fibers to be excluded have either too few steps to form a feasible tract, tracked to the wrong side of the aponeurosis or ended prematurely due to very high curvature or FA values outside the TA range. Reasonable TA tracts are expected to extend fully from the aponeurosis to the muscle border, with the exception of a few voxels due to partial volume artifacts. Anatomical MR images with higher resolution than DTI provide more certain boundaries, therefore it is possible for the tracts to end just before reaching the exact boundary. Tracts are typically formed forward from a seed point, following the PDD along consecutive voxels until current FA extends a pre determined range or successive points have higher curvature than a preset threshold. Multiple experiments carried out plantarflexion, neutral position and dorsiflexion of the leg have shown a suitable FA range to be (0.15, 0.75) and a maximum curvature of 45° for fiber termination [14–16]. The repeatability of DTI-based fiber tracking in skeletal muscles is confirmed by DAI, pennation angle and fiber tract length measurements through four acquisitions on two days that allowed for between acquisitions in identical positions, within day acquisitions after repositioning and between days analyses [14, 40].

2.3.2. Muscular Force Transmission

Skeletal muscles are surrounded by a fascia, which is a flat sheet of connective tissue separating different tissue layers, and also a further connective tissue known as the epimysium. The muscle itself consists of smaller structural units called fascicles, in which muscle bundles are formed from muscle fibers. Each fascicle is surrounded by perimysium, again a type of connective tissue. The individual muscle fibers exist within a cell membrane called the sarcolemma, and each fiber is surrounded by the endomysium, a thin sheet of connective tissue. Muscle fibers operate within this endomysial structure resembling tunnels. The smallest contractile unit in a muscle is referred as the sarcomere, composed of myofilaments responsible from the muscle function. Sarcomeres are arranged in series along a muscle fiber, and in parallel within adjacent fibers of fascicles and bundles.

Muscle activity is based on the generation and transmission of force, resulting in length changes of muscle units under constant muscle volume. Length-force and force-velocity characteristics are determined to investigate the structure and function of distinct muscles. In classical muscle mechanics, myotendinous junctions located at the ends of muscle fibers and the aponeuroses are considered to be the exclusive sites of force transmission. In such myotendinous transmission, force is transmitted to bone without leaving the muscle-tendon complex bounded by the epimysium (muscle fascia) and epitenon (tendon fascia). Within the classical approach of muscle activity studies, muscle force was measured by fully dissecting the target muscle, except for its innervation and blood supply, and the muscle force was measured at one tendon. This approach isolates the muscle from its surroundings and implicitly assumes that the force measured at one tendon is equal to the force exerted at the other end, and length force characteristics of the studied muscle are unique to that muscle. On the contrary, recent *in vivo* studies in which the muscle is and its surroundings are left intact, show that muscle relative position is important and the length force characteristics are not unique [9]. Moreover, the forces exerted at the origin and insertion of a muscle are not equal, and in the microscopic level sarcomere lengths show remarkably heterogeneous distribution. These results are linked to a different pathway of force transmission called the myofascial force transmission, which occurs between all muscles within a limb segment.

The notion of myofascial force transmission points out that muscles are not mechanically independent units from each other or their surroundings, the force generated within sarcomeres of an antagonistic muscle may be exerted at the tendon of target muscle or its synergists [6]. The role of direct and indirect intermuscular connections in muscular force transmission are highlighted in recent studies indicating the force is not exclusively transmitted to the origin or insertion of the muscle fibers but also onto the endomysium and further onto the intramuscular connective tissue stroma, where endomysial, perimysial and epimysial tunnels within which muscle fibers, fascicles and the whole muscle are active. Less than half but substantial amount of the total force transmission occurs myofascially [6].

Intramuscular myofascial force transmission can be present in the form of shearing, where the intramuscular stroma acts as a single deformable element that lengthens and shortens during contractions, and the total diameter of the element increases or decreases because the muscle volume remains constant. The force transmission between a muscle and its immediate surrounding tissues is epimuscular myofascial force transmission. Epimuscular myofascial force transmission is either intermuscular, between linked intramuscular stromata of two synergistic muscles, or extramuscular, from a muscle onto extramuscular tissues. Any myofascial force transmission between antagonistic muscles or muscle groups involves extramuscular myofascial connections.

Leaving the epimuscular connections intact and measuring the forces exerted at both proximal and distal tendons yield proximo-distal force differences in length force characteristics of a muscle. In fully isolated conditions ruling out epimuscular force transmission, the proximally and distally directed forces are expected to be equal. Epimuscular force transmission imposes a net additional load onto the muscle in either direction. Experiments performed on the extensor digitorum longus (EDL) muscle of the rat in intact condition (TA and extensor hallucis longus (EHL) present as synergistic muscles) and with extramuscular connections exclusively (TA and EHL removed) prove that muscle optimal length is different for the two cases as well as the amount difference between the proximo distal forces. The shift of muscle optimal length suggests an increased heterogeneity in the length of sarcomeres. In determining the sarcomere length, the interaction of sarcomeres in series has to be taken into consideration along with the parallel arrangement and the forces exerted onto the sarcomere by the extracellular matrix. In

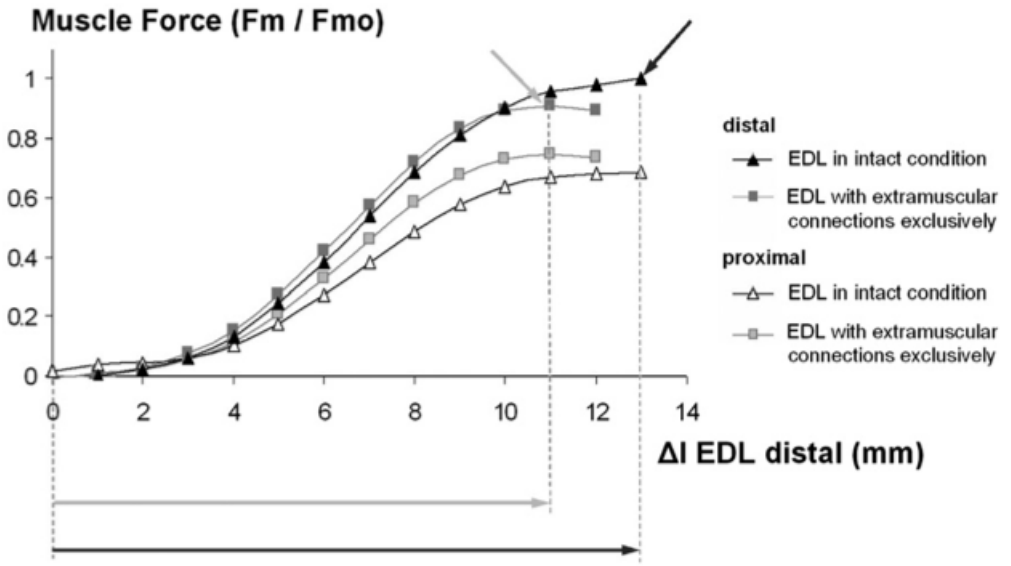

Figure 2.3. Effects of different myofascial components of epimuscular force transmission on EDL isometric muscle length-force characteristics. The length-force characteristics of EDL with intact inter and extramuscular connections is compared to those of the isolated muscle, with TA and EHL removed and only extramuscular connections present [9].

addition, epimuscular loads distributed non uniformly onto the muscle epimysium affect the sarcomere lengths, again, in a non uniform fashion. Because any sarcomere shortens until it equilibrates with the imposed load, sarcomeres exposed to myotendinous plus myofascial loads are expected to be longer than sarcomeres exposed only to a similar myotendinous load, since myofascial load is not exerted homogeneously. Fiber strain analyses performed on EDL estimate different local sarcomere lengths within fibers. Further research on gastrocnemius shows that although the global strain within a muscle is zero in isometric conditions, much higher local strains may occur due to myofascial connections. Moreover, this local strain distribution is not limited to GM itself but was carried onto the synergistic soleus (SOL) muscle. In fact, myofascial force transmission is active for all muscle groups within the lower limb, regardless if they are antagonistic or synergistic muscles [7].

Upon any length change, the position of the muscle with respect to the fixed bony structures will change, as well as amount of direct intermuscular connections of adjacent muscles. These, in turn, lead to alterations in extramuscular connections and the epimuscular loads. Therefore along with muscle length, relative position becomes a major determinant of force

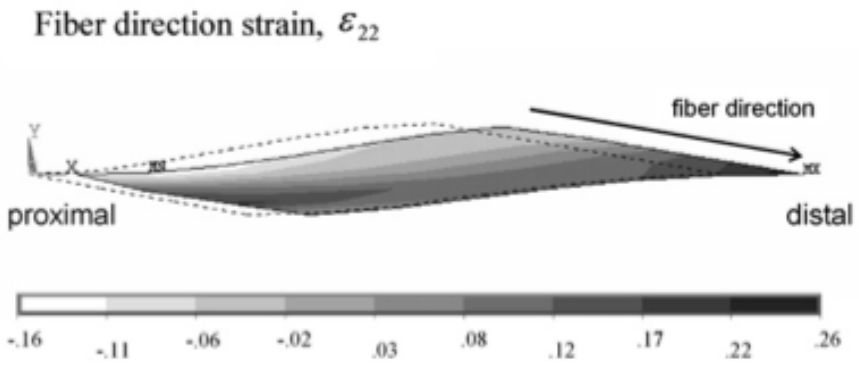

Figure 2.4. Distributions of fiber strain along EDL with extramuscular connections exclusively. Positive and negative strains indicate lengthening and shortening of the sarcomeres with respect to their original length, respectively. Sarcomeres arranged in serial distribution are considered for analysis [9].

and hence it is crucial to enhance *in vivo* methodologies in skeletal muscle characterization.

2.3.3. DT-MRI and Strain Tensor Analyses on Skeletal Muscles

The discovery of heterogeneously distributed local fiber strains along proximal and distal ends of human GM muscle is a major influence for the need to carry out advanced research studying the strain in the direction of muscle fibers, representing length changes of sarcomeres. Studies have indicated that the intramuscular patterns of strain development during contractions are not only spatially heterogeneous but also multidimensional, hence the local fiber geometry must be taken into consideration [7]. The resulting strain in any muscle activity can be characterized in the form of a symmetric second-order tensor just like the diffusion tensor, where the diagonal elements represent the normal and off-diagonal elements represent the shear strains at a given voxel. The eigenanalysis of the strain tensor reveals the principal strain directions and the associated magnitudes, where the direction of the eigenvector associated with the largest positive eigenvalue, ε_P, is the direction of maximum elongation and denoted as $\vec{u_P}$ and the direction of the eigenvector associated with the negative eigenvalue having the largest absolute value, ε_N, represents the direction of maximum shortening and is denoted as $\vec{u_N}$.

In both superficial and deep compartments of human TA muscle, the direction of ε_N

was closest to, but deviated from, the fiber direction. The elevation angle for $\vec{u_N}$ differed significantly from the elevation angle of $\vec{v_1}$ but their azimuth angles were almost the same. The direction of ε_P was mostly closest to $\vec{v_2}$, with their elevation angles again significantly different yet, their azimuth angles were matching [41].

The directional strain analysis is highly informative on the structural and functional characteristics of the muscle. For instance the intercompartmental differences between ε_P and ε_N are likely to emerge from the difference between the material properties of the fiber origins in the superficial and deep compartments of TA, since the pennation angles and fascicle lengths are similar and both sets share a common aponeurosis and tendon of insertion [7]. It is known that the superficial compartments originate from a more compliant structure. Most importantly, the reported differences in strain magnitudes point out to developed shear strains on the central aponeurosis.

Another indication of shear stress within the muscle is highlighted from the fact that $\vec{u_N}$ and $\vec{v_1}$ are not colinear, where $\vec{v_1}$ parallels the fiber direction. The deviation of $\vec{u_N}$ away from $\vec{v_1}$ was attributed to the heterogeneity in fiber length and pennation within the superior and inferior portions of TA itself [41–44]. The close alignment of $\vec{u_P}$ and $\vec{v_2}$ may suggest the existence of some higher order aspect of muscle architecture in determining the principal elongation direction, but the details of such proposed relationship is yet to be inspected. The comparison of diffusion and strain tensor elements connect the effects of myofascial force transmission within the structure-function relationship of skeletal muscles *in vivo*. This connection constitutes the main biomechanical basis for this thesis.

3. METHODOLOGY

Muscle deformation assessment is carried out using two types of analyses involving the spatial distribution of diffusion and strain characteristics within the base and deformed configurations of the lower leg. The main two components constructing the base of both analyses are the tractography process, which constitutes the coordinate frame of spatial analysis, and the displacement field which maps the deformed configuration voxels onto the base configuration to explore the changes in the diffusion characteristics and the resulting strain from the deformation.

3.1. Data Loading and Object Representation

In order to investigate both the diffusion and strain statistics along the skeletal muscles within different positions and contraction schemes of the leg, two separate datasets are needed. Both MRI acquisitions are performed on the same physical segment on the leg and the only difference in the protocol is that in one the knee is bent and the leg is flexed with 150° angle between femur and tibia, and in the other the leg is extended as the angle is brought to 180°. Each volume consists of the same number of axial slices of identical size stacked on top of each other, with the resolutions of both of the volumes also identical. A typical diffusion weighted image (DWI) set consists of G continuous stacks of N slices each, where G represents the number of gradient directions in acquisition plus one (non-directional $b = 0$) and N is the number of anatomical slices constituting the volume. In other words, each of the N slices have G number of images, $G - 1$ of them are directional. In choosing the gradient directions, no two directions should be parallel and no four should be coplanar. As stated before, at least six directions are needed for the construction of the diffusion tensor. If any three vectors are coplanar then the remaining vectors must be linearly independent. It is generally optimal to choose the gradient directions so as to separate uniformly in space and there is no universally accepted way to compare the effectiveness of different sampling schemes [17].

Once the data is loaded, the diffusion tensors are constructed using the attenuation Equation 1.2 and 1.3. Each volume is stored in a DTIData object which can hold the following

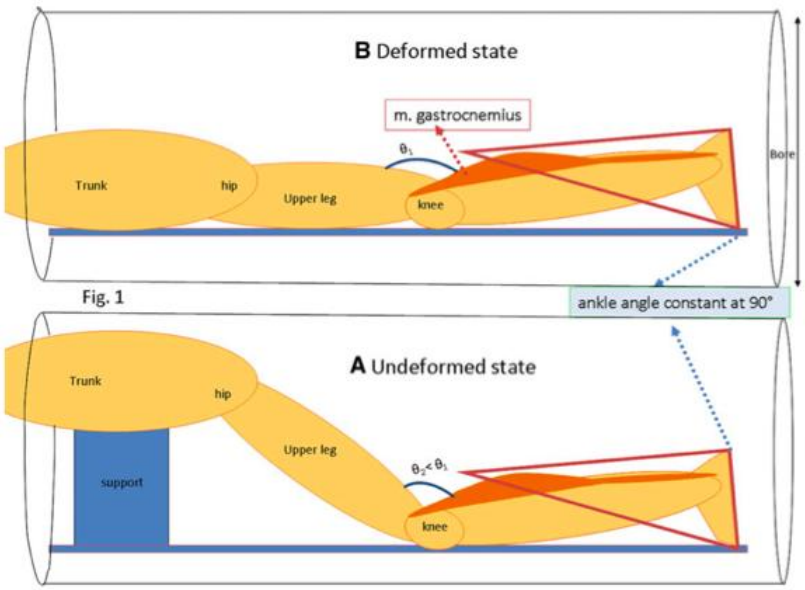

Figure 3.1. Schematic representation of the experimental setup within the MRI machine. Subject position is prone with the ankle angle fixed to 90°. Undeformed and deformed states represent the flexed and extended configurations, respectively. Undeformed knee joint angle $\approx 180°$, deformed knee joint angle $\approx 150°$ [6].

variables for:

(i) For each voxel:

- Diffusion tensor elements for each voxel: $[D_{xx}\, D_{yy}\, D_{zz}\, D_{xy} D_{xz}\, D_{yz}]$
- Diffusion tensor eigenvalues for each voxel: λ_1, λ_2, λ_3
- Diffusion tensor eigenvectors for each voxel: $\vec{v_1}$, $\vec{v_2}$, $\vec{v_3}$
- Strain tensor elements for each voxel: $[E_{11}\, E_{22}\, E_{33}\, E_{12}\, E_{13}\, E_{23}]$
- Strain tensor eigenvalues for each voxel: ε_1, ε_2, ε_3
- Strain tensor eigenvectors for each voxel: $\vec{u_1}$, $\vec{u_2}$, $\vec{u_3}$
- Displacement vector (for mapping of voxels)
- Scalar indices FA, ADC

(ii) For the whole data:

- Visualization volume (b0 or anatomical MRI)
- Fiber tracts

Data size, resolution and gradient encoding scheme with the b-values are read from the

data and stored.

3.2. Displacement Field Computation

The displacement field **u** is the 3D vector field which maps the position of any base (flexed position) voxel to the corresponding deformed (extended position) as in Figure 2.1. In order to compute the displacement field, DT and MR images of volumes of both configurations are used. Including MR images in the computations is beneficial because of their higher resolution, which yields more accurate mappings of voxels.

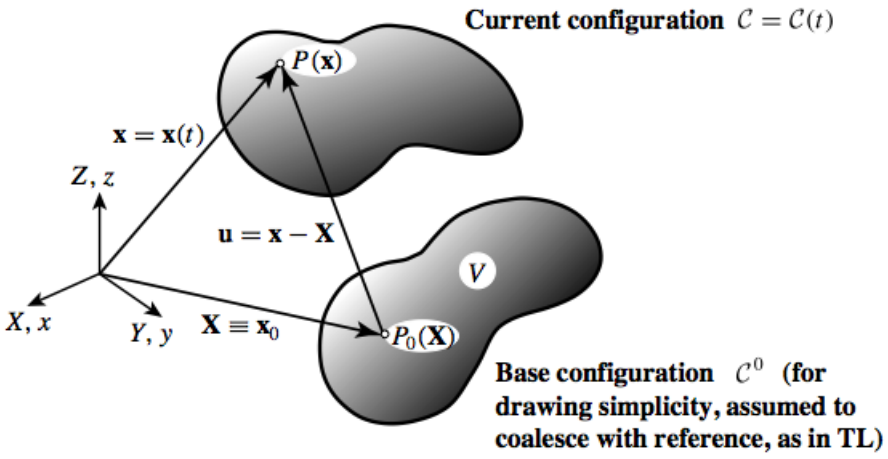

Figure 3.2. The geometric representation of the mapping between the base (flexed) and deformed (extended) configurations of the data. **u** is the displacement vector [45].

The first step of the mapping procedure is aligning the DTI and MRI datasets (shown as transformations ψ_b and ψ_d in Figure 3.3 for the mapping of the base and deformed configurations, respectively) using a landmark based affine transformation to compensate for any possible motion effects between DTI and MRI acquisitions. Following this alignment stage, the direction convention of MR images were matched with that of the DT images, MRI volumes were cropped to contain the physical space of DT images with a ±30mm buffer zone. To prevent data loss, spacing was left unchanged. All alterations performed on MR images were applied simultaneously to minimize resampling artifacts.

After aligning the DTI and MRI datasets, the MRI dataset of the deformed configuration was registered onto the MRI dataset of the base configuration by a deformable registration

algorithm, denoted as T in Figure 3.3, which constitutes two steps: a rigid registration for bulk motion and an elastic stage using the Demons algorithm [46]. The first step used sum of differences algorithm with a 4×4 rigid transformation matrix. The rigidity assures that no strain is imposed during registration. The output transform of step one was used to obtain the vector field of displacements, which was used as an initial guess in the second step, elastically deforming the images for further matching. The shape change between the two configurations is addressed within this stage, hence all the strain is imposed in the second step. The final result (depicted as transformation T^* in Figure 3.3) is the displacement field $\mathbf{u}$ mapping voxel-to-voxel motion from the base to the deformed MRI configurations, which also maps the base DTI configuration to the deformed DTI configuration, only at a higher resolution.

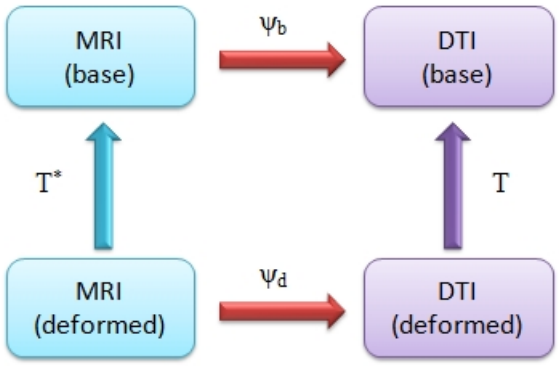

Figure 3.3. Flowchart of the transformations involved in the displacement field computations. DTI and MRI alignment of the base and deformed data are denoted as ψ_1 and ψ_2, respectively. MRI to MRI registration is shown as T^*. The final mapping is denoted as T.

Since the DTI and MRI datasets were aligned previously, high resolution displacement field obtained from MRI datasets can be used to compute the displacement of any voxel in DT images.

3.3. Deformation Field and Strain Tensor Field Computation

In continuum mechanics, deformation refers to the change of metric properties of a body. This change can be exemplified as the length change of any curve within the body from a reference configuration to a deformed configuration. If there is no length change between the two placements, i.e. there is no relative displacements between the body particles after the displacement of the continuum, then only rigid body motion is present and no deformation

occurs. For deformation analysis, the position vector of any particle in base (X) and deformed configurations (x) are referred to as the material and spatial coordinates, respectively. Deformation analysis can be carried out in terms of either the material or spatial coordinates, where our calculations are based on the material coordinates, also referred as the Lagrangian description.

In continuum mechanics, strain is a representation of deformation referring to the relative displacement of particles with the rigid body motions excluded. This exclusion is ensured by calculating strain as a quantity relative to a reference length, hence strain measures point out how much a given deformation differs locally from a rigid body deformation [47]. Strains are in general expressed as tensor quantities like the diffusion tensor, and can be decomposed into its normal and shear components. A typical strain tensor is depicted as:

$$\mathbf{E} = \begin{bmatrix} e_{11} & e_{12} & e_{13} \\ e_{21} & e_{22} & e_{23} \\ e_{31} & e_{32} & e_{33} \end{bmatrix} \tag{3.1}$$

with the elements of the diagonalized tensor representing the normal strain, i.e. strain in the orthogonal directions constituting the reference frame of the tensor, and the off diagonal elements represent the shear strains, which can be interpreted as the sliding of layers over one another and are represented as the change in angles between any two of the originally orthogonal segments intersecting at a point. Biological soft tissue deformations involve arbitrarily large rotations and strains where the undeformed and deformed configurations of the continuum are significantly different, unlike materials exhibiting elastic behavior such as concrete or steel. This type of large deformations are classified as components of finite strain theory, on which the following computations are based [45].

The transformation

$$\mathbf{x} = \mathbf{X} + \mathbf{u} \tag{3.2}$$

maps the position of the base voxel $P(X, Y, Z)$ to $P(x, y, z)$. The displacement vector in

Lagrangian description is hence:

$$\mathbf{u} = \begin{bmatrix} u_1 \\ u_2 \\ u_3 \end{bmatrix} = \begin{bmatrix} x - X \\ y - Y \\ z - Z \end{bmatrix} = \mathbf{x} - \mathbf{X} \tag{3.3}$$

where (x, y, z) and (X, Y, Z) correspond to the same physical location within the two data. If a computed point in the deformed configuration is off-grid in the low resolution DT images, linear interpolation is performed to obtain the displacement vector.

The derivatives of (x, y, z) with respect to (X, Y, Z) arranged in Jacobian format constitute the deformation gradient tensor:

$$\mathbf{F} = \frac{\partial(x, y, z)}{\partial(X, Y, Z)} = \begin{bmatrix} \frac{\partial x}{\partial X} & \frac{\partial x}{\partial Y} & \frac{\partial x}{\partial Z} \\ \frac{\partial y}{\partial X} & \frac{\partial y}{\partial Y} & \frac{\partial y}{\partial Z} \\ \frac{\partial z}{\partial X} & \frac{\partial z}{\partial Y} & \frac{\partial z}{\partial Z} \end{bmatrix} \tag{3.4}$$

The material displacement gradient tensor with respect to the reference configuration is represented as:

$$\nabla u = \mathbf{F} - \mathbf{I} = \begin{bmatrix} \frac{\partial x}{\partial X} - 1 & \frac{\partial x}{\partial Y} & \frac{\partial x}{\partial Z} \\ \frac{\partial y}{\partial X} & \frac{\partial y}{\partial Y} - 1 & \frac{\partial y}{\partial Z} \\ \frac{\partial z}{\partial X} & \frac{\partial z}{\partial Y} & \frac{\partial z}{\partial Z} - 1 \end{bmatrix} = \begin{bmatrix} \frac{\partial u_x}{\partial X} & \frac{\partial u_x}{\partial Y} & \frac{\partial u_x}{\partial Z} \\ \frac{\partial u_y}{\partial X} & \frac{\partial u_y}{\partial Y} & \frac{\partial u_y}{\partial Z} \\ \frac{\partial u_z}{\partial X} & \frac{\partial u_z}{\partial Y} & \frac{\partial u_z}{\partial Z} \end{bmatrix} \tag{3.5}$$

Green-Lagrange strain tensor is one of the multiple representations of material strain, convenient in expressing large local deformations:

$$\mathbf{E} = \begin{bmatrix} e_{11} & e_{12} & e_{13} \\ e_{21} & e_{22} & e_{23} \\ e_{31} & e_{32} & e_{33} \end{bmatrix} = \frac{1}{2}(\mathbf{F}^T\mathbf{F} - \mathbf{I}) \tag{3.6}$$

Rotation of the strain tensor can be used to calculate principal strains by the removal of shear effects. The first and third principle strains represent local lengthening and shortening,

respectively [6, 7].

3.4. Tractography

The term tractography refers to the technique used to construct the fibrous architecture within bodily structures using DTI data. The elements of computer based image analysis for this construction here are the fiber tracts which are three dimensional parametrized curves proceeding iteratively, where complete tracts are formed by the interpolation of consecutive tract voxels. Fiber tracts throughout the TA muscle are constructed using the 4^{th} order Runge-Kutta integration based streamline algorithm described in [48]. The intermediate points following the seed point of a tract are determined by interpolating the DTI data in three dimensions using a linear Lagrange interpolating polynomial and the major diffusion vector is then calculated as from a continuous, normalized vector field [48]. The step direction to each new tract point is thus computed by recursively computing the principal diffusion direction of the voxels involved in the interpolating polynomial and normalized step vectors connect the consecutive points of a tract.

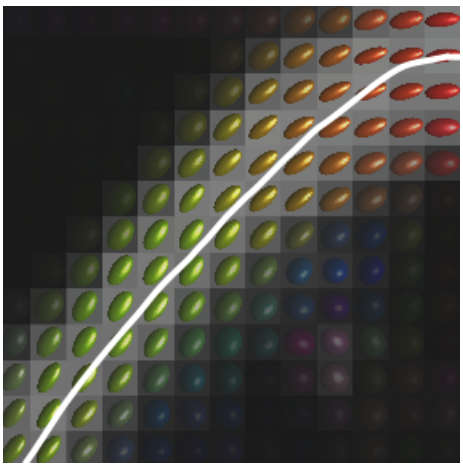

Figure 3.4. The output tract of a PDD based streamline tractography algorithm. Principal diffusion directions are the long axes of the diffusion ellipsoids colored according to tensor orientation (red for horizontal axis, blue for vertical axis, green for surface normal direction) [49].

An individual tract starts from a seed voxel and proceeds forward and backward in two distinct loops until a stopping condition is reached in any direction. The forward and backward

tracts are merged at the end, forming a complete tract from a single seed point. The step size at each iteration is chosen as half of the smallest voxel dimension. Seed points are determined within a certain range of FA values, the whole data FA is sorted from largest to smallest and the seed points with the highest FA values are picked one by one, until all have been traced and no more seeds are left to process. The typical FA seed range is experimentally determined as $[0.1, 0.5]$ along the TA fibers. The algorithm stops and returns a complete tract if any of the following conditions occur while proceeding:

- Current FA value exceeds the defined range,
- Current curvature exceeds a defined threshold,
- Current tract length exceeds a defined maximum tract length,
- Current voxel reaches the data boundaries.

where the curvature is the angle (in degrees) between the previous direction and the step direction within the algorithm. Once a tract is completed, it can be stored in the DTIData object.

In order to carry out an analysis of the spatial distribution of strain and diffusion characteristics, the fiber tracts within a selected region of interest are chosen as a fiber frame of reference. It was stated before that the DTI based fiber tractography outputs correlate with the local fiber orientations, therefore the fiber tracts elongating through a given region of interest represent individual skeletal muscle fibers. For analysis of the strain and diffusion characteristics along the tracts, the direction of the tract at a voxel of interest has to be computed. This direction highly correlates with the principal diffusion direction, since the principal diffusion direction of a voxel influences the tractography step, however, the two directions are not necessarily identical. The tract direction at a given tract voxel is determined as the normalized tangent of the vector joining the backward and forward adjacent points to that voxel, and denoted as $\vec{t}$.

3.5. Diffusion Analysis

The parameters involved in the analysis of the spatial distribution of diffusion characteristics in base configuration are the diffusion anisotropy indices FA, ADC (as in Equations 2.5 and 2.6, respectively) and the linear diffusion coefficient (LDC), which is the scalar diffusion parameter *along* the tract direction and is computed as:

$$LDC = \vec{t}^T \mathbf{D} \vec{t} \tag{3.7}$$

FA measures the fraction of anisotropy at a given voxel and ranges between 0 (completely isotropic diffusion) and 1 (completely anisotropic diffusion), ADC or the mean diffusivity represents the total diffusivity with the effects of anisotropy averaged out, LDC represents the diffusivity along the tract direction.

While these three indices computed along the base configuration tracts represent the diffusion characteristics of the flexed muscle fibers, a comparison based on the same indices of the deformed configuration fiber tracts is carried out in terms of the Δ parameters. Specifically, for each voxel in the base configuration, the corresponding voxel in the deformed configuration is located using the displacement field as in Equation 3.2. The difference of FA, ADC and LDC values between extended and flexed configurations, respectively, are computed to determine the amount of change in the spatial distribution of diffusion characteristics. LDC parameter of a deformed voxel is calculated along the direction of the tract passing though the deformed voxel. This small tract consisting of a minimum of three points is formed by choosing the deformed voxel of concern as the seed point. The deformed tract tangent is the normalized adjoining vector of the previous and following tract voxels.

$$\begin{aligned} \Delta FA &= FA_{ext} - FA_{flx} \\ \Delta ADC &= ADC_{ext} - ADC_{flx} \\ \Delta LDC &= LDC_{ext} - LDC_{flx} \\ &= \vec{t}^T_{ext} \mathbf{D}_{ext} \vec{t}_{ext} - \vec{t}^T_{flx} \mathbf{D}_{flx} \vec{t}_{flx} \end{aligned} \tag{3.8}$$

where subscripts ext and flx denote the deformed and base configuration parameters, respectively. Here, the deformed configuration voxel does not have to coincide with a grid point. If the deformed point is indeed an off grid point, the diffusion tensor has to be interpolated via 8-point neighbor interpolation. Since diffusion tensors are symmetric positive semi-definite, with nonnegative eigenvalues, Log-Euclidean framework is preferred [50]. Once a diffusion tensor is diagonalized, computing the matrix exponential or the matrix logarithm is equivalently carried out by simply computing the exponential or the logarithm of the diagonal matrix elements. The interpolated off-grid tensor is:

$$\overline{\mathbf{D}}_{ext} = exp\left(\sum_{i=1}^{8} w_i log(\mathbf{D}_{ext_i})\right) \tag{3.9}$$

where w_i are the normalized weights ascribed to each neighboring tensor, inversely proportional to the physical distance between the off-grid point and the i^{th} neighbor voxel, and $\mathbf{D}_{ext_i}$ is the diffusion tensor at the i^{th} neighbor in the deformed configuration. FA_{ext}, ADC_{ext} and LDC_{ext} are not interpolated individually but computed using $\overline{\mathbf{D}}_{ext}$ for the diffusion tensor and its eigenvalues in Equations 2.5, 2.6 and 3.7.

The Δ parameters in Equation 3.8 represent how the physical deformation from the movement of the leg from flexed to extended position changes the diffusion characteristics, thereby reflect the microstructural changes within the tissue. Any change in FA, ADC or LDC identify the local alterations of the muscular architecture. Rather than the voxel-wise changes of the Δ parameters it is important to investigate how the Δ parameters are distributed in the longitudinal and axial directions so that the effects of deformation on microstructure can be analyzed. Specifically, any heterogeneous pattern in the distribution of Δ parameters along the fibers and within the axial muscle boundaries would hint heterogeneous structural changes at the microscopic level within the sarcomeres.

3.6. Strain Analysis

Strain analysis is carried out by computing the strain tensor at each voxel of the base configuration and extracting the strain coefficient (SC) at each voxel along the tract direction:

$$SC = \vec{t}^{T}\mathbf{E}\vec{t} \tag{3.10}$$

As the tractography step size is half the smallest dimension of a voxel, off-grid strain tensors have to be interpolated. Having both positive and negative eigenvalues, strain tensor interpolation cannot be carried out via logarithmic computations. Instead, linear interpolation based on the weighted means of the grid neighbors of a given voxel is used:

$$\overline{\mathbf{E}} = \sum_{i=1}^{8} w_i \mathbf{E}_i \tag{3.11}$$

where w_i are the normalized weights ascribed to each neighboring tensor, inversely proportional to the physical distance between the off-grid point and the i^{th} neighbor voxel, and $\mathbf{E}_i$ is the diffusion tensor at the i^{th} neighbor.

The strain tensor at a given voxel expresses the changes in length of the local muscle tissue or fibers as a result of the motion from flexed to extended configuration. The deformation changes the local sarcomere lengths and also the relative position of the muscle with respect to its surroundings as well as te intermuscular connections. It is therefore important to investigate the distribution pattern of strain along the fibers, both in terms of the longitudinal distribution in between muscle ends and also within the axial planes. Heterogeneous strain coefficients would suggest heterogeneous lengthening or shortening at the sarcomere level. This, in turn, would hint that the loads resulting from the deformation are unequally distributed onto different locations of the muscle, pointing at the effects of myofascial force transmission.

3.7. Statistical Analysis

The main goal of the statistical analysis is to assess longitudinal and lateral heterogeneities within the spatial distributions of strain and diffusion characteristics along the TA muscle fibers as the movement of the lower leg imposes a structural deformation.

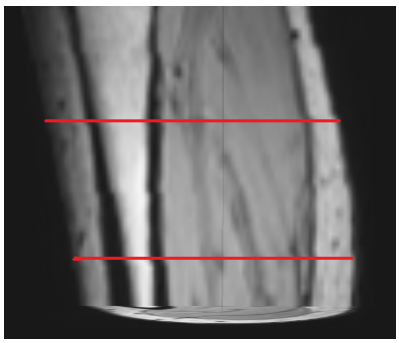

Figure 3.5. Typical proximo-distal range of the analyzed fibers for the three subjects, depicted on the anatomical dataset of the third subject. Left side of the figure is anterior, bottom is distal.

The fibers included in the detailed analysis were chosen to elongate through the distal and proximal muscle ends; two polygonal regions of interest (ROI) were defined toward the distal and proximal ends of the base (flexed) dataset and tracts elongating through both polygons were selected for evaluation. The appropriate ROI concerning the TA muscle were determined empirically, within confidence regions of the anterior crural department such that the EDL and EHL muscles, tibia and fibula bones, nerves and the aponeurosis were excluded. From the bipennate structure of the TA, only the posterior portion of the muscle is included due to the aponeurosis exclusion and curvature limitations.

In order to achieve the heterogeneity assessment, each measured parameter (FA, ADC, LDC, Δ parameters and SC) along each voxel is plotted versus the horizontal axis representing the tract steps. Horizontal ground level (zero) corresponds to the mid point between each chosen ROI pair, with the left and right of the horizontal axis representing the more distal and proximal ends of the muscle, respectively.

After each fiber parameter is computed, a longitudinal averaging is performed by averaging the parameter value through all fibers at a given horizontal step. This averaging represents the

entire collection of parameters onto a single plot denoted as m, characterizing the longitudinal distribution of the parameter of concern. At each horizontal step, computation of the standard deviation of the entire fiber collection from the parameter average m at the horizontal step of concern yields another distribution denoted as s, which characterizes the lateral distribution of each parameter. All calculations are carried out within a confidence region where 80% of all fibers are present for robust modeling.

The average m and the standard deviation s of a given parameter along the fibers can both be modeled as Gaussian distributions with distinct means and standard deviations as model parameters. For a given set of fibers, the standard deviation $\sigma(m)$ of the longitudinal average curve modeled as a Gaussian $\mathcal{N}_m(\mu(m))\sigma(m)$ represents to what extent the parameter is distributed heterogeneously along fibers, i.e. proximo-distal axis. The mean $\mu(s)$ of the standard deviation curve modeled as a Gaussian $\mathcal{N}_s(\mu(s), \sigma(s)))$, on the other hand, expresses the extent of heterogeneity of the parameter's distribution on a given axial slice, within fibers at consecutive steps. $\sigma(m)$ and $\mu(s)$ are therefore the indicators of longitudinal and lateral heterogeneity of the distribution of the measured parameters, respectively, within the entire fiber collection. Relatively large values of $\sigma(m)$ and $\mu(s)$ express higher degrees of longitudinal and lateral spreads, which points out to local structural heterogeneities as a result of the deformation. $\sigma(m)$ and $\mu(s)$ are also used for inter subject analysis, in comparing the lateral and longitudinal distribution of parameters between different subjects.

3.8. Visualization

Fibers were visualized via colormaps specifying the LDC and SC distributions, where each voxel is assigned a color based on the parameter value. For longitudinal assessment, color assignment is carried out within step size resolution along base configuration tracts. The colormap ranges are identical with the range of the parameter to be visualized. For lateral assessment, the parameter of concern is averaged within the confidence interval along each fiber and the associated colormap is based on the range of the entire collection of fiber averages. These average values are then mapped onto each individual fiber of the associated subject to indicate the lateral spread of fiber averages.

3.9. Datasets

Studies were performed on three female volunteers, all with healthy knee and ankle joints and feet. None of the subjects were exposed to heavy training or muscle pain prior to the experiments. Subjects ages were between 25 and 28 (with mean 26.67 ± 1.53 years), weights: 60.33 ± 4.51 kilograms and heights 160.67 ± 8.50 centimeters.

All subjects laid in prone position during both the undeformed and deformed state image acquisitions, as depicted previously in Figure 3.1. The angle between the upper leg and the lower leg is approximately 150° for the flexed configuration and 180° for the extended configuration, where the subject position in flexed state was fixed using an apparatus that elevates and supports the trunk. The ankle angle is fixed at 90°. Subjects' legs were strapped onto the surface with velcro tape and additional straps were used to fix the upper body. The experiments were conducted with %0 maximum voluntary contraction (MVC), i.e. under passive conditions.

The data were obtained with a Siemens 3T Magnetom Trio Scanner using two surface coils. Anatomical reference images were acquired from a Turbo Flash scan with the following parameters: echo time TE = 3.36ms, repetition time TR = 1750ms, matrix size $320 \times 320 \times 128$, voxel size $1 \times 1 \times 1 mm^3$, interslice gap 1mm. The diffusion weighted images were obtained in 12 continuous stacks of 40 slices each, using a single shot echo-planar imaging (ss-EPI) sequence with the following parameters: TE = 61ms, TR = 3700ms, matrix size $128 \times 128 \times 40$, voxel size $1.4 \times 1.4 \times 2.8 mm^3$ and interslice gap 2.8mm. A 5/8 Fourier acquisition was used along the phase-encode direction. The b-value for the ss-EPI sequence was $450 s/mm^2$, number of gradient directions is 12, number of excitations N_{EX} is 5. Fat suppression was performed using inversion recovery (Fat SAT). All experiments were performed in Acibadem Kozyatagi Hastanesi, Istanbul.

4. RESULTS

4.1. Spatial Distribution of Diffusion Anisotropy Indices and Δ Parameters

Figures 4.1 through 4.3 depict the FA, ADC, LDC and ΔFA, ΔADC and ΔLDC parameters, averaged over all fibers within the confidence range, for subjects 1 through 3, respectively. No significant trends similar for all subjects is observed, as intersubject variability is expected due to many reasons including subject physiology and muscular development. Local fluctuations in the spatial distribution of diffusion anisotropy indices and Δ parameters are indicative of structural differences at sarcomere level along fibers.

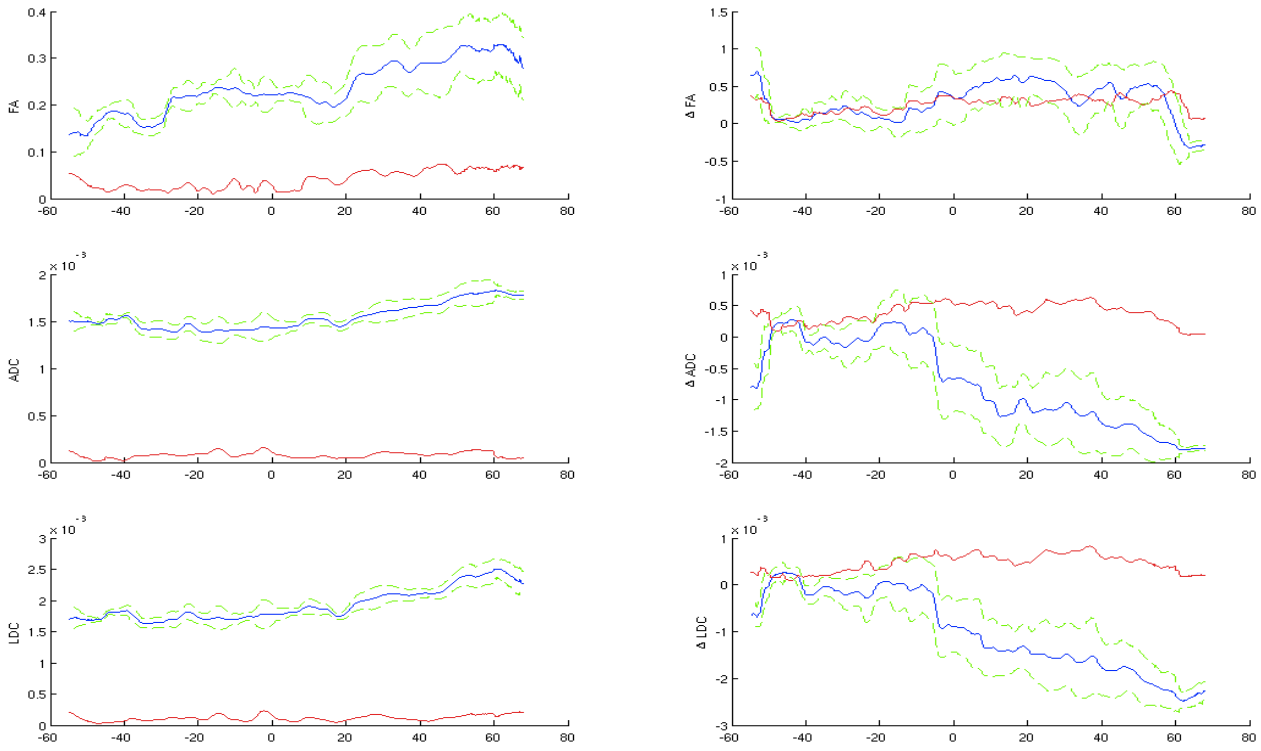

Figure 4.1. FA, ADC, LDC (right column, top to bottom) and ΔFA, ΔADC, ΔLDC (left column, top to bottom) along fiber tracts of Subject 1, averaged over all fibers (blue). Red plots indicate the standard deviation of m, green curves represent $m \pm s$ (blue ± red). Horizontal axis represents tract steps from distal to proximal ends.

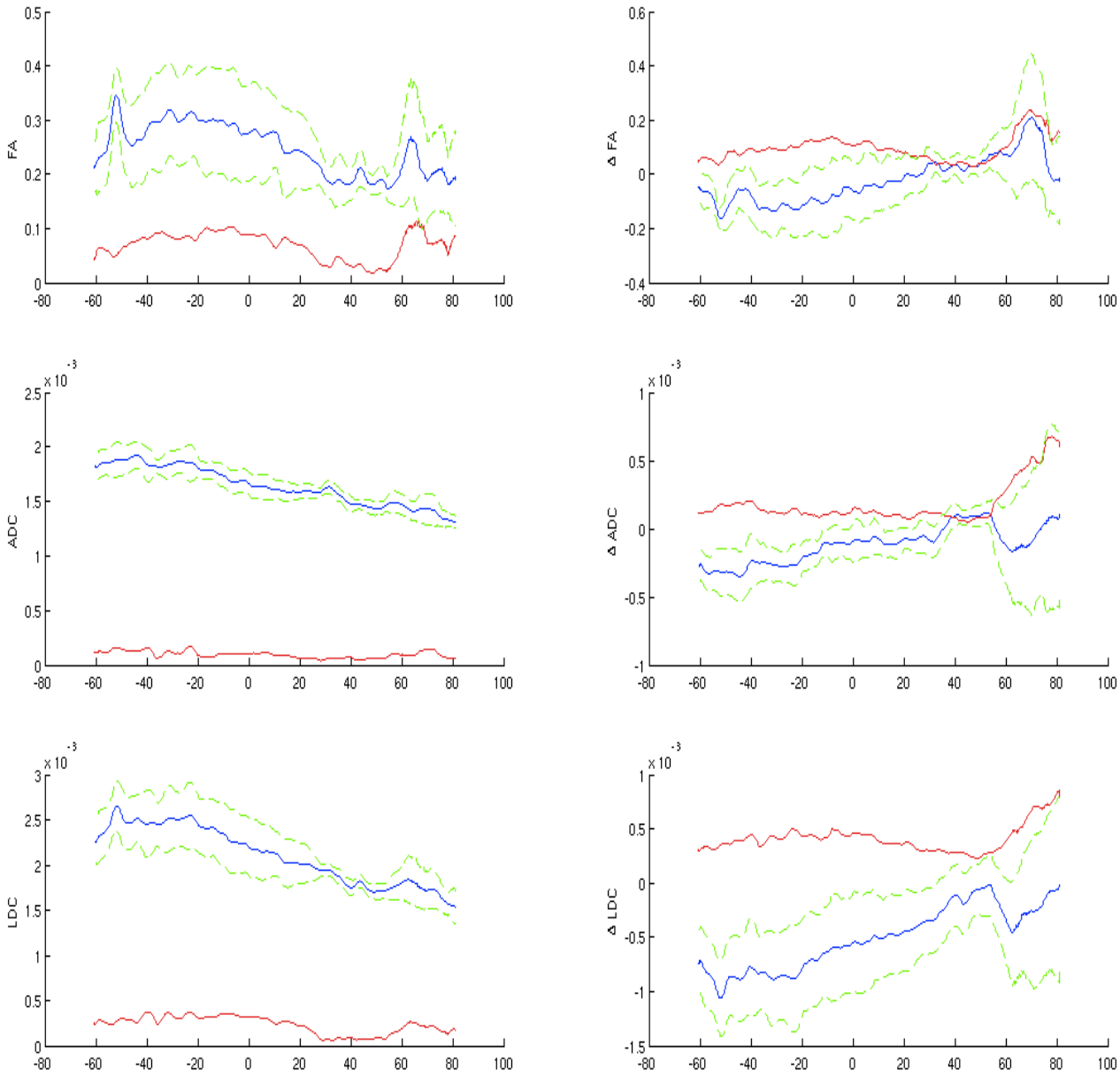

Figure 4.2. FA, ADC, LDC (right column, top to bottom) and ΔFA, ΔADC, ΔLDC (left column, top to bottom) along fiber tracts of Subject 2, averaged over all fibers (blue). Red plots indicate the standard deviation of m, green curves represent $m \pm s$ (blue $\pm$ red). Horizontal axis represents tract steps from distal to proximal ends.

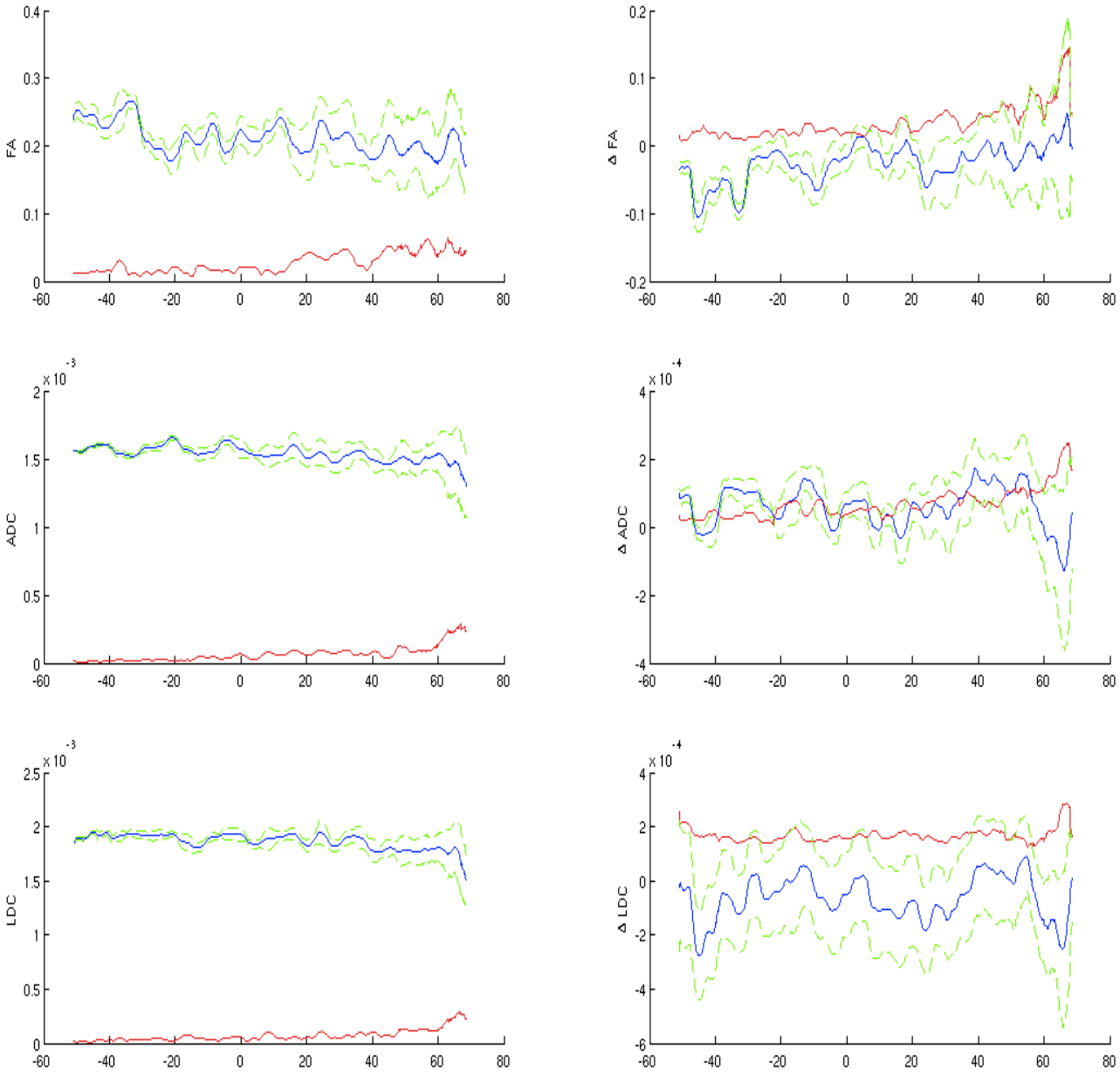

Figure 4.3. FA, ADC, LDC (right column, top to bottom) and ΔFA, ΔADC, ΔLDC (left column, top to bottom) along fiber tracts of Subject 3, averaged over all fibers (blue). Red plots indicate the standard deviation of m, green curves represent $m \pm s$ (blue $\pm$ red). Horizontal axis represents tract steps from distal to proximal ends.

In Figure 4.4, the distribution of LDC along fibers is visualized using colormaps within the regions of interest of all subjects. The LDC visuals show both the global and local changes of diffusivity along the fiber direction and it can be seen that proximo-distal differences as well as local increases and decreases of diffusivity are present. While Figure 4.4 represents the longitudinal assessment of structural heterogeneities in terms of the diffusion parameters, Figure 4.5 is representative of the heterogeneities in diffusivity along fiber direction between adjacent fibers within the regions of interest.

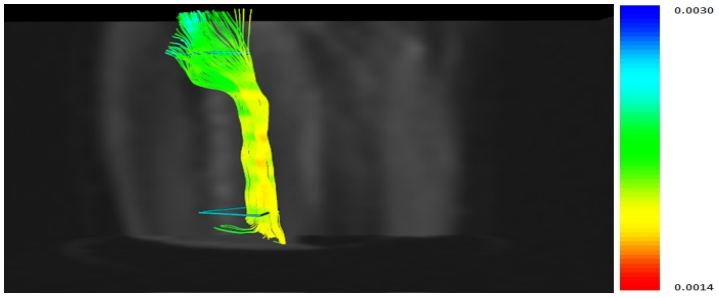

(a) Subject 1

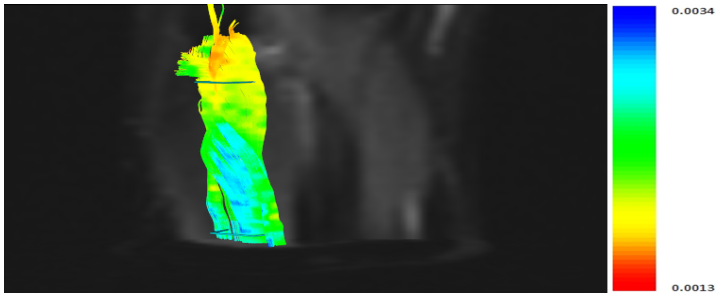

(b) Subject 2

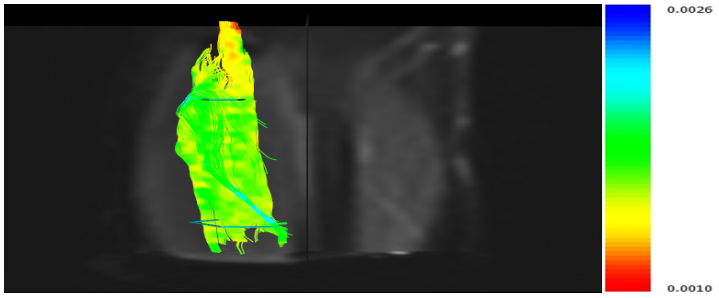

(c) Subject 3

Figure 4.4. LDC distirbutions along fibers for Subjects 1, 2 and 3, from top to bottom, respectively. Colormap ranges are identical with the global LDC ranges for all subjects.

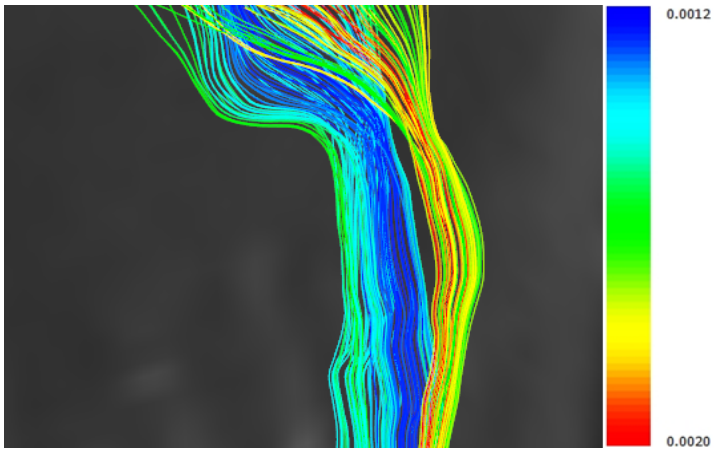

(a) Subject 1

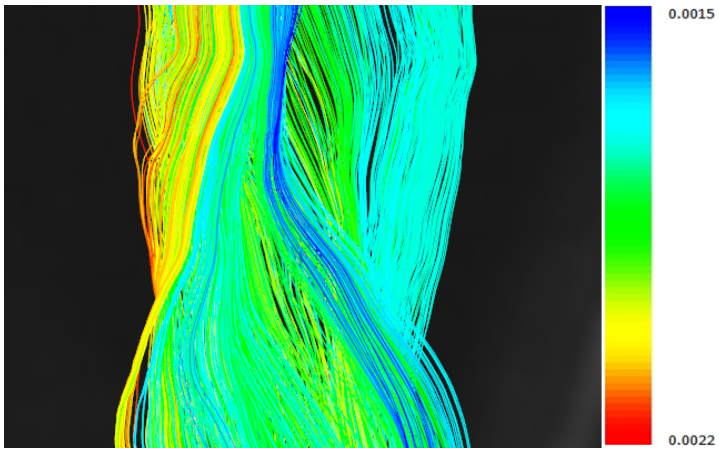

(b) Subject 2

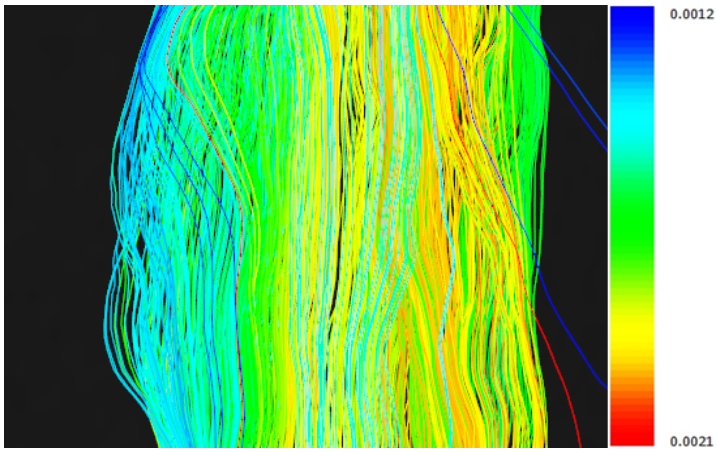

(c) Subject 3

Figure 4.5. LDC averages of each fiber within the confidence range depicted with a single color along fibers for Subjects 1, 2 and 3, from top to bottom, respectively. Colormap ranges are identical with the global LDC average ranges for all subjects.

4.2. Spatial Distribution of Strain

Figure 4.6 depicts the SC plots for all subjects, where both proximo-distal as well as local differences in strain distributions can be traced. Figure 4.7 shows how variable the mean strain of individual fibers differ from each other at each step of fiber tracts. Again, the former figure shows how heterogeneously strains are distributed longitudinally within fibers, whereas the latter highlights the lateral heterogeneities. A flat line would be observed in Figure 4.7 if equal mean strains were present along adjacent muscle fibers.

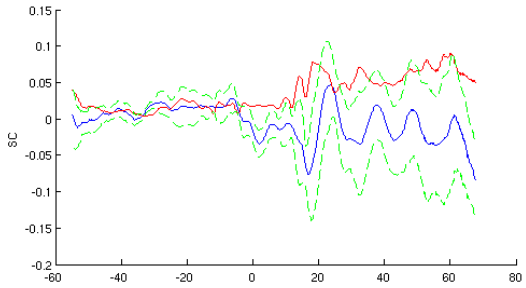

(a) Subject 1

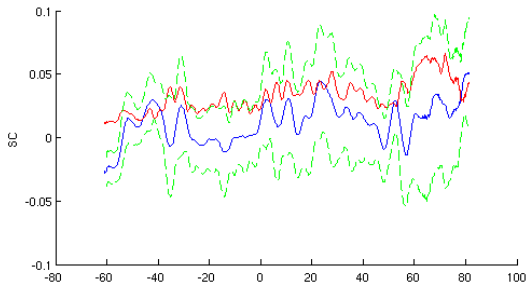

(b) Subject 2

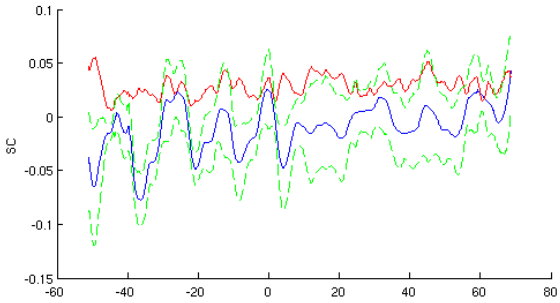

(c) Subject 3

Figure 4.6. SC along fiber tracts of Subjects 3, 4 and 5 from top to bottom, respectively, averaged over all fibers (blue plots). Red plots indicate the standard deviation of associated average curves, green curves represent $m \pm s$ for each subject. Horizontal axis represents tract steps from distal to proximal ends.

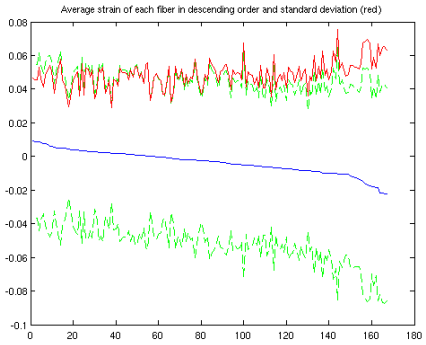

(a) Subject 1

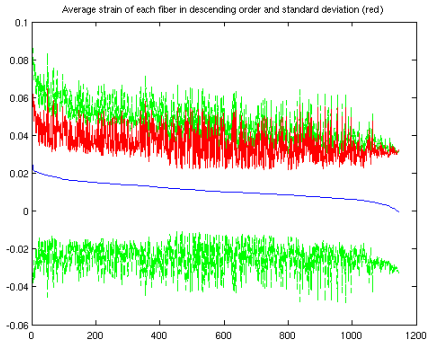

(b) Subject 2

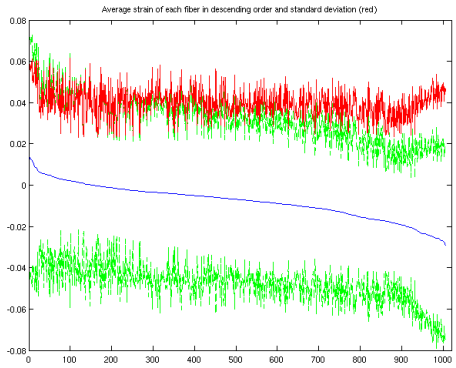

(c) Subject 3

Figure 4.7. Average strain of each fiber presented in descending order (blue) with their standard deviations(red) for Subject 1(a), Subject 2(b) and Subject 3(c). Green plots represent average values ± standard deviation for each fiber. Horizontal axis represent fiber numbers included in the analysis.

The findings are also visualized for each fiber in Figure 4.8. The TA muscle has no insertion at the knee joint but is connected to the ankle, however the ankle angle is fixed for both positions of the leg. Changing the knee angle between the two configurations results in global strains clustered around zero, yet sarcomeres are both lengthened and shortened locally along fibers, indicated by positive and negative strains, respectively. Figure 4.9 show these heterogeneities within the lateral distribution, where the mean fiber strains are different for individual muscle fibers.

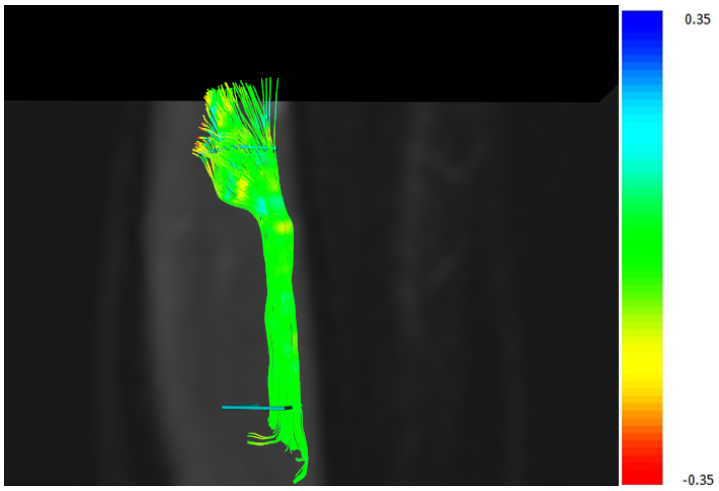

(a) Subject 1

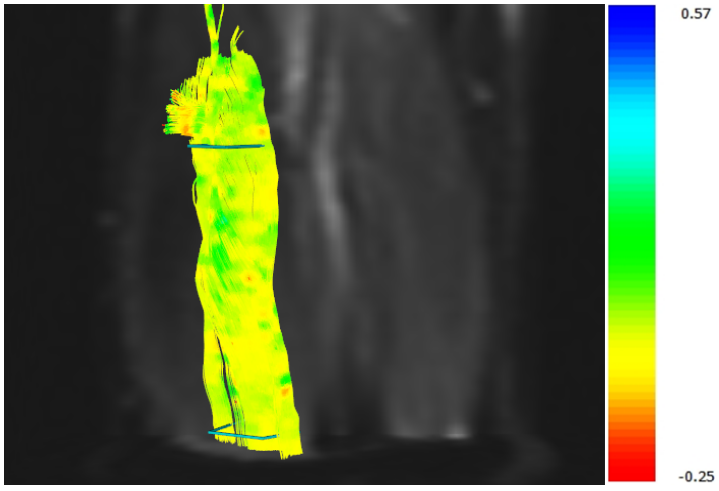

(b) Subject 2

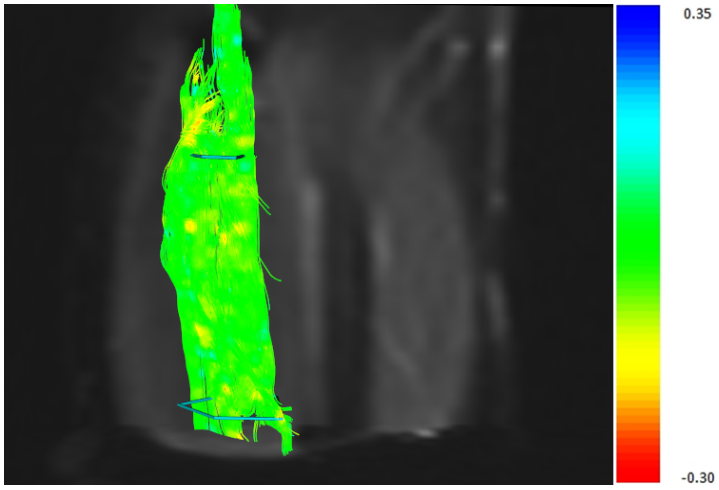

(c) Subject 3

Figure 4.8. SC distirbutions along fibers for Subjects 1, 2 and 3, from top to bottom, respectively. Colormap ranges are identical with the global SC ranges for all subjects.

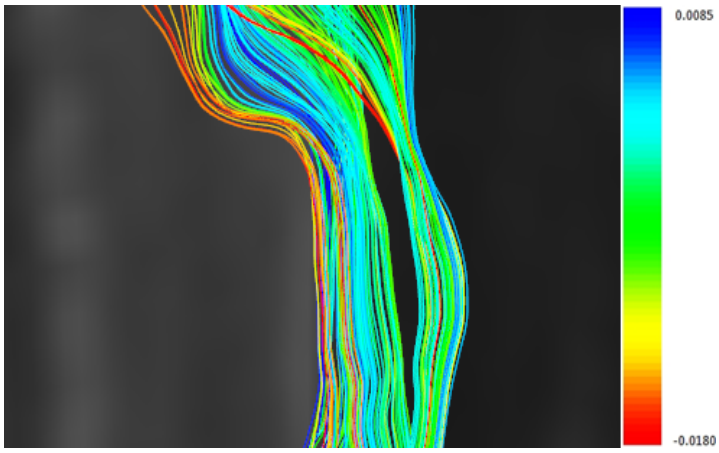

(a) Subject 1

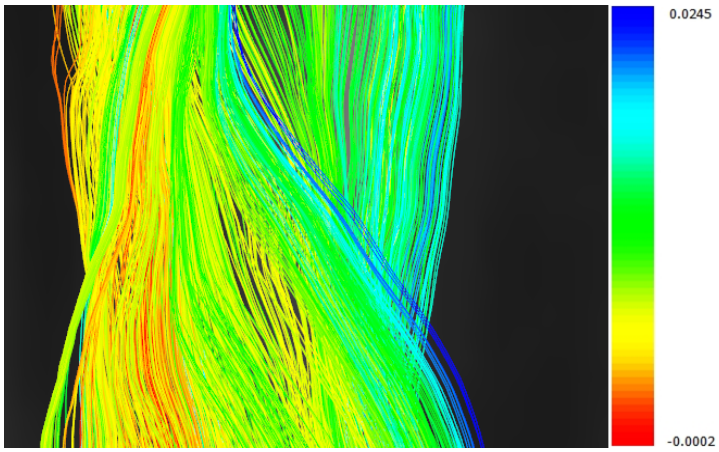

(b) Subject 2

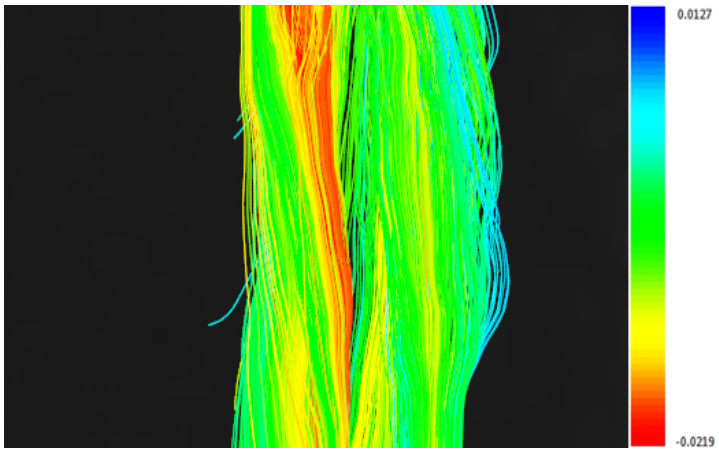

(c) Subject 3

Figure 4.9. SC averages of each fiber within the confidence range depicted with a single color along fibers for Subjects 1, 2 and 3, from top to bottom, respectively. Colormap ranges are identical with the global LDC average ranges for all subjects.

4.3. Longitudinal Heterogeneity Assessment for Spatial Distribution of Diffusion and Strain Characteristics

For each measured parameter, the longitudinal analysis is performed by modeling the parameter average m (i.e. m_{FA}, m_{ADC}, m_{LDC}, $m_{\Delta FA}$, $m_{\Delta ADC}$, $m_{\Delta LDC}$, m_{SC}) over all fibers elongating within the confidence region as a Gaussian distribution $\mathcal{N}_m(\mu(m), \sigma(m))$. The spread of the Gaussian probability density function $\sigma(m)$ is an indicator of how much the selected index varies along the fibers, i.e. the heterogeneity of the index values paralleling fiber direction.

As seen on Figure 4.10, for the diffusion anisotropy indices subjects 1 and 2 have similar and larger spreads compared to subject 3. The Δ parameters on the other hand, are similar for subejcts 2 and 3 but subejct 1 has a larger degree of heterogeneity in terms of the spatial distribution. For the strain coefficient, however, all subjects have comparable longitudinal heterogeneities. The statistical results are listed in Table 4.1. Though the numerical values are not high, $\mu(m)$ and $\sigma(m)$ are mostly of same order of magnitude for the Δ parameters and strain coefficient.

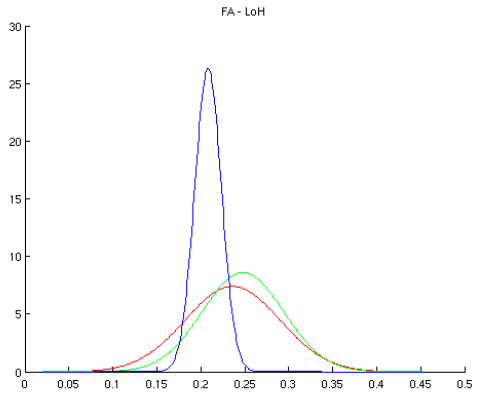

(a) FA

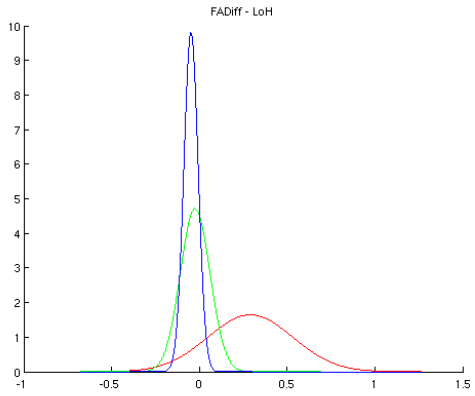

(b) ΔFA

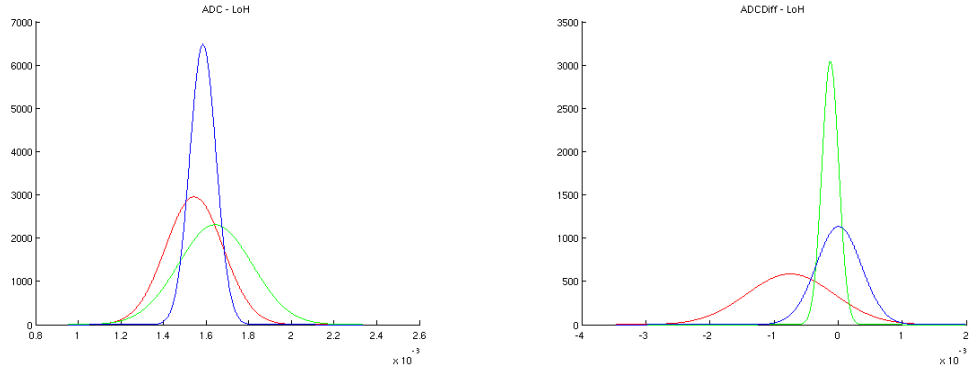

(c) ADC (d) ΔADC

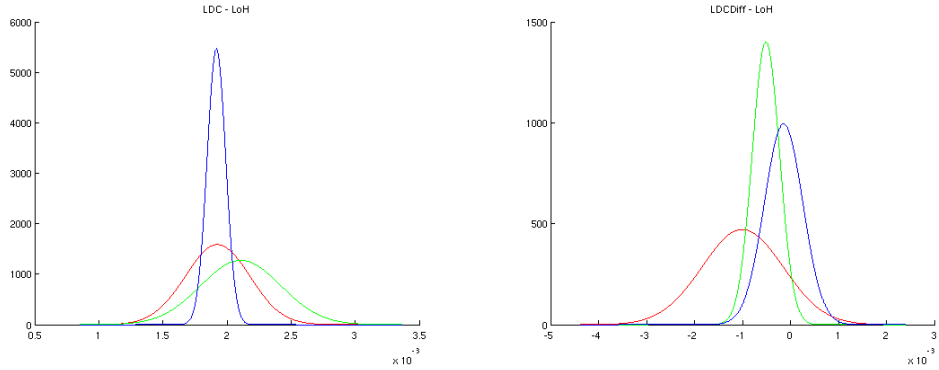

(e) LDC (f) ΔLDC

Figure 4.10. Longitudinal analysis plots of (a)FA, (b)ΔFA, (c)ADC, (d)ΔADC, (e)LDC and (f)ΔLDC for Subjects 1(red), 2(green) and 3(blue). Plots represent the Gaussian distribution models of the fiber average curves m.

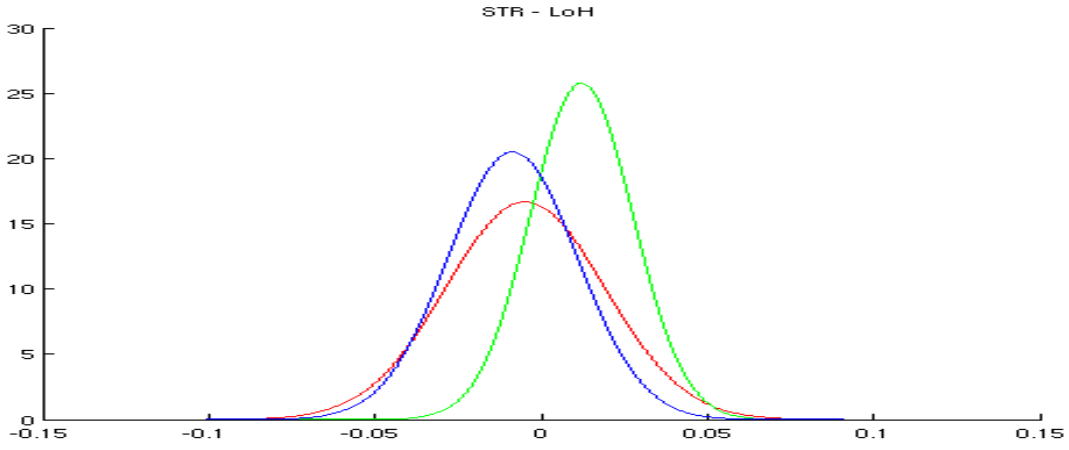

Figure 4.11. Longitudinal analysis plots SC for Subjects 1(red), 2(green) and 3(blue). Plots represent the Gaussian distribution models $\mathcal{N}_m(\mu(m), \sigma(m))$ of the fiber average curves m.

Table 4.1. Parameters of $\mathcal{N}_m(\mu(m), \sigma(m))$ for longitudinal heterogeneity assessment, for all measurements over all subjects.

	$\mu(m) \pm \sigma(m)$		
Subject	1	2	3
FA	0.2362 ± 0.0539	0.2479 ± 0.0464	0.2117 ± 0.0220
ADC ($\times 10^{-3}$)	1.5728 ± 0.1350	1.6283 ± 0.1727	1.5342 ± 0.5218
LDC ($\times 10^{-3}$)	1.9324 ± 0.2514	2.1020 ± 0.3133	1.9223 ± 0.6774
ΔFA	0.2932 ± 0.2426	-0.0233 ± 0.0845	-0.0262 ± 0.0282
ΔADC ($\times 10^{-3}$)	0.7375 ± 0.6809	-0.1202 ± 0.0680	0.0595 ± 0.0590
ΔLDC ($\times 10^{-3}$)	-0.0995 ± 0.0846	-0.5105 ± 0.2846	-0.0645 ± 0.0080
SC	-0.0047 ± 0.0239	0.0122 ± 0.0155	-0.0104 ± 0.0224

4.4. Lateral Heterogeneity Assessment for Spatial Distribution of Diffusion and Strain Characteristics

For each measured parameter, the lateral analysis is performed by modeling the parameter standard deviation s (i.e. s_{FA}, s_{ADC}, s_{LDC}, $s_{\Delta FA}$, $s_{\Delta ADC}$, $s_{\Delta LDC}$, s_{SC}) over all fibers elongating within the confidence region as a Gaussian distribution $\mathcal{N}_s(\mu(s), \sigma(s))$. Lateral analysis measures the extent of heterogeneity of each parameter of concern within fibers at the same axial proximity. The mean of the distribution, $\mu(s)$, represents how much each parameter deviates along different fiber tract voxels sharing the same axial coordinates.

The extent of lateral heterogeneity for all subjects is more similar for the diffusion anisotropy indices compared to the Δ parameters, the effects of inter subject variability is more dominant in the right column of Figure 4.12, as the muscle configuration is changed. The longitudinal heterogeneity of subject 1 was highest in terms of DAI but from the lateral perspective subject 1 has the most homogeneous spatial distribution. Again for the strain coefficient all subjects have almost identical lateral heterogeneities, which is seen in Figure 4.13 and depicted in Table 4.2. As in the case of longitudinal heterogeneity assessment, the values presented in Table 4.2 are low but indicative of local fluctuations of the measured parameters among adjacent fibers at consecutive tract steps.

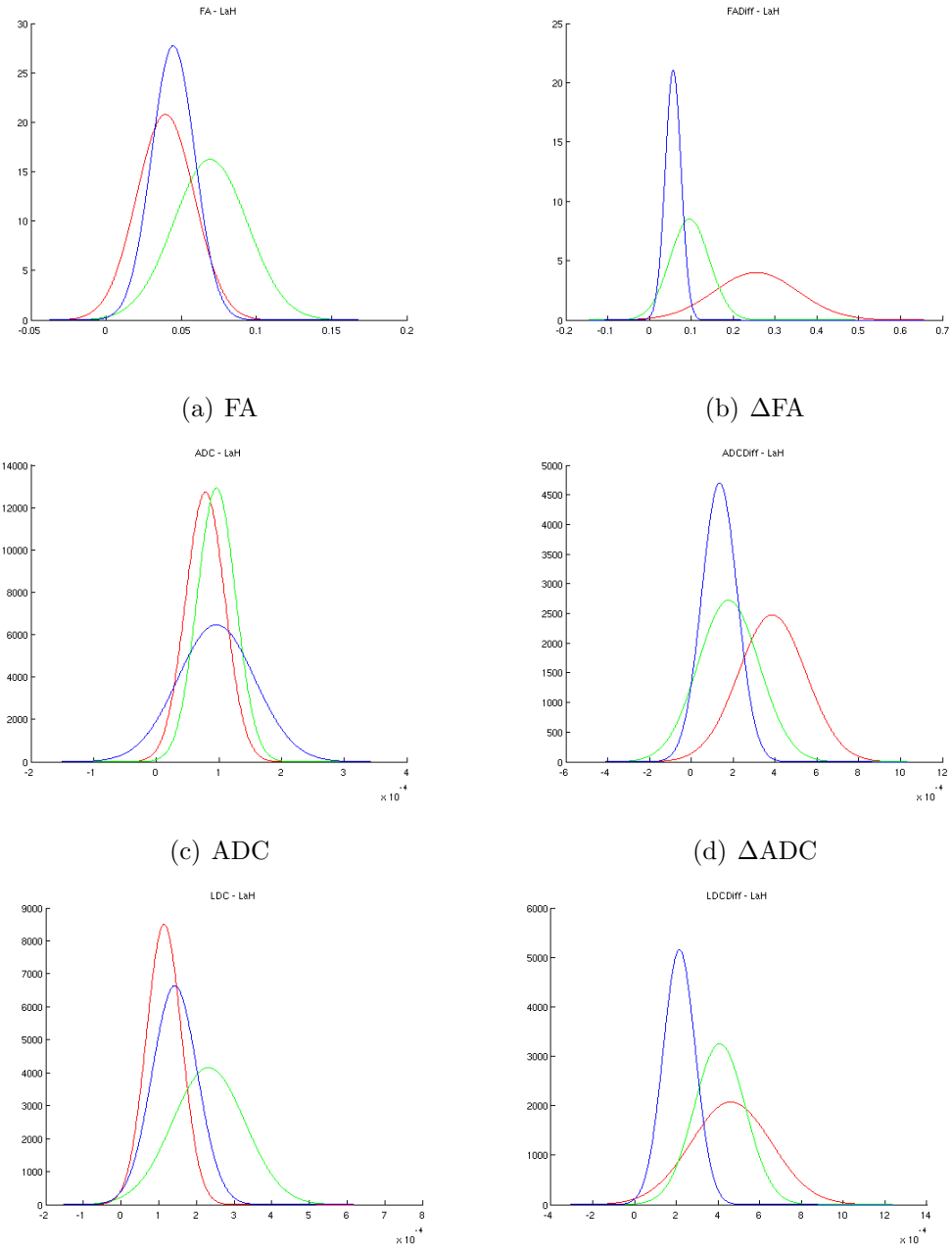

(a) FA (b) ΔFA

(c) ADC (d) ΔADC

(e) LDC (f) ΔLDC

Figure 4.12. Lateral analysis plots of (a)FA, (b)ΔFA, (c)ADC, (d)ΔADC, (e)LDC and (f)ΔLDC for Subjects 1(red), 2(green) and 3(blue). Plots represent the Gaussian distribution models $\mathcal{N}_s(\mu(s), \sigma(s))$ of the fiber average curves s.

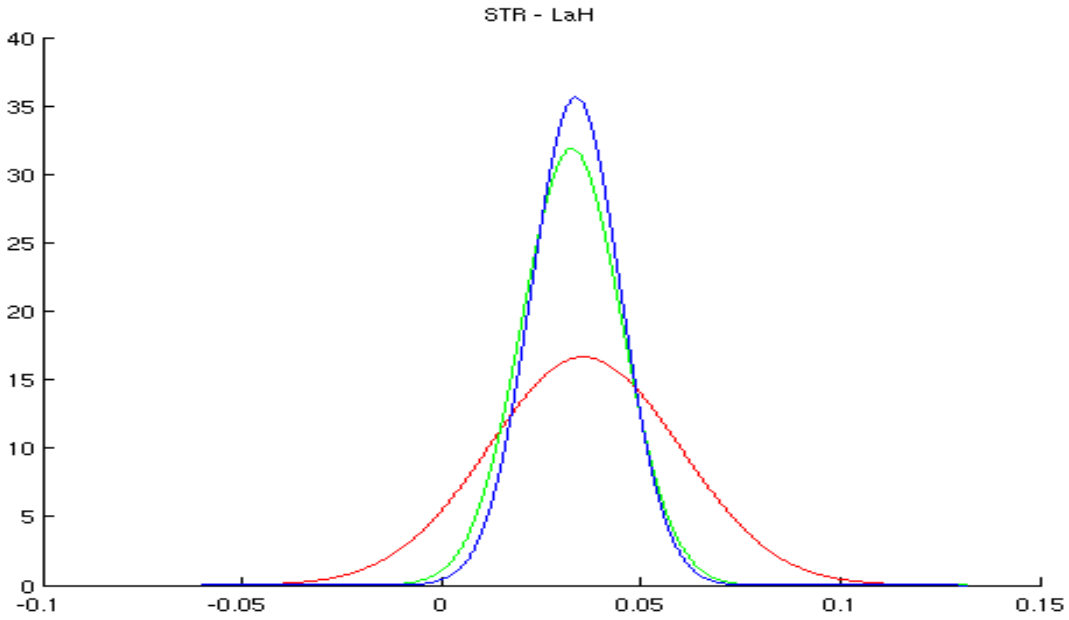

Figure 4.13. Lateral analysis plots SC for Subjects 1(red), 2(green) and 3(blue). Plots represent the Gaussian distribution models $\mathcal{N}_s(\mu(s), \sigma(s))$ of the fiber average curves s.

Table 4.2. Parameters of $\mathcal{N}_s(\mu(s), \sigma(s))$ for lateral heterogeneity assessment, for all measurements over all subjects.

	$\mu(s) \pm \sigma(s)$		
Subject	1	2	3
FA	0.0396 ± 0.0192	0.0694 ± 0.0246	0.0271 ± 0.0146
ADC ($\times 10^{-4}$)	0.7841 ± 0.3133	0.9662 ± 0.3086	0.6447 ± 0.5475
LDC ($\times 10^{-4}$)	1.1409 ± 0.4691	2.3263 ± 0.9603	7.0716 ± 0.5350
ΔFA	0.2559 ± 0.0998	0.0960 ± 0.0469	0.0333 ± 0.0094
ΔADC ($\times 10^{-4}$)	3.8685 ± 1.6111	1.7817 ± 1.4642	0.6679 ± 0.4275
ΔLDC ($\times 10^{-4}$)	4.6297 ± 1.9228	4.0847 ± 1.2263	1.6708± 0.2467
SC	0.0358 ± 0.0240	0.0327 ± 0.0125	0.0287 ± 0.0094

5. DISCUSSION

5.1. Spatial Distribution of Diffusion and Strain Parameters through Fiber Average Plots

Figures 4.1 through 4.3 depict the diffusion anisotropy indices at base configuration and the difference of the same indices between the base and deformed configurations averaged over all fibers within the confidence region of Subjects 1, 2 and 3, respectively. From the distal end of the TA fibers to the proximal end, FA values along the fiber tracts of Subject 1 under undeformed conditions show an increasing trend. Standard deviation of the FA values at each step of tracts also increase slightly toward the proximal end, indicating a larger lateral heterogeneity of FA values between fibers. ADC and LDC values tend to increase toward both distal and proximal ends in a parallel fashion, with low variances. Subject 2 has a higher FA variance along the tracts compared to Subject 1 and the FA values seem to be decreasing slightly toward the proximal end except for an increasing pattern at the very end of the confidence region. ADC and LDC values of Subject 2 decrease along the distal proximal direction. Subject 3 has a more fluctuating FA pattern between the two ends, neither increasing nor decreasing from one end to the other, and again a slightly decreasing pattern for both ADC and LDC indices.

The Δ plots in figures 4.1 through 4.3 represent the changes in the diffusion anisotropy indices from the base configuration to the deformed configuration. Subject 1 has a mostly increasing FA average over all fibers. At regions where FA increases the most, ADC and LDC values decrease and vice versa. This result conforms the most with the expected results, since the deformed position of the leg is considered to have elongated fibers compared to the flexed position. Increased fractional anisotropy toward the fiber direction, and as a result lower ADC, are therefore hypothesized. Subject 2 has a much smaller FA difference between the two configurations, which is similar for ADC and LDC. In addition, on average subject 2 shows increasing trends for all DAI measured between each configuration. For Subject 3, FA indices have been reduced globally, but again with local fluctuations. ADC and LDC changes are not dramatic, though LDC changes are slightly larger than ADC.

It is important to highlight that the difference fiber plots are indicative of spatial heterogeneities within the index distributions. The fluctuations depict that contrary to a globally constant trend, the diffusion parameters are changing with local differences. The deformation induced by the movement of the leg seems to have caused heterogeneous alterations within the muscular microstructure.

Strains along the fibers for Subject 1 tend to cluster with small fluctuations around zero close to the distal end, yet the fluctuations become larger toward the proximal end of the muscle. Fluctuations with much higher frequencies along the distal proximal range is observed for the remaining subjects, with no significant global trend of increasing or decreasing strains. Instead, both positive and negative strains are observed as consecutive steps are followed tracing the fibers. Again, just like the change in the diffusion parameters, the fact that the imposed strains possess a fluctuating character points out to the presence of a heterogeneous distribution of loads as a result of the deformation in all three subjects.

5.2. Longitudinal Assessment

The longitudinal assessment plots of the diffusion parameters are shown in Figure 4.10. The first two subjects have higher DAI spreads compared to the third in base configuration, indicating that the diffusion parameter changes along each fiber on the longitudinal axis of the former are higher than the latter. The ΔFA between the two configurations has the largest spread for Subject 1, longitudinal heterogeneity for the same parameter decreases for Subjects 2 and 3. ΔADC and ΔLDC longitudinal heterogeneity is again dominant for Subject 1, followed by subjects 3 and 2.

All three subjects present a comparable longitudinal heterogeneity in terms of the strain along the fibers, shown in Figure 4.11. Figure 4.7 can also be used to assess longitudinal heterogeneities in strain distribution on fibers, depicting the average longitudinal strains assigned to each each fiber, sorted and plotted with respect to fiber indices. It can be seen that there is a slight change of mean fiber strain between individual fibers for all three subjects. Although the range is small, with a maximum of 0.0315 for Subject 1, it is plausible to suggest that the strain distribution along the muscle fibers in microscopic scale possesses a heterogeneous

character.

Table 4.1 depicts the distribution parameters of all diffusion anisotropy indices, Δ parameters and SC averaged over all fibers for the three subjects. As stated previously, the indicative parameter for the longitudinal analysis is the standard deviation of the indices. For all subjects, LDC and ΔLDC standard deviations ($\sigma(m_{LDC})$ and $\sigma(m_{\Delta LDC})$) are higher compared to ADC and ΔADC deviations ($\sigma(m_{LDC})$ and $\sigma(m_{\Delta LDC})$), meaning that the diffusivity along the main fiber axis is distributed non uniformly between voxels, as well as the change in the diffusivity along the fiber direction from base to deformed configurations. Strain coefficient is the only index having the same order of magnitude for the mean and variance of average distributions, indicating that the longitudinal strain heterogeneity can be considered more significant. The deviations of $\sigma(m)$ of the diffusion anisotropy indices and diffusion Δ parameters on the other hand, are much smaller. This is because along the fibers the diffusion of water molecules is unconstrained at the fiber resolution, independent of the configuration as long as a dominant fiber orientation is present. Linear diffusion coefficients not along the fiber tract direction but along the remaining orthogonal directions, however, could be more indicative in deformation analysis since the second and third eigenvectors of the diffusion tensor have been associated with fiber cross section. The constraint here is that the low resolution of DT-MR imaging is inadequate in implying linear diffusion index changes originating from fiber cross section alterations.

5.3. Lateral Assessment

Among the three subjects, subject 2 has the highest axial FA spread,$\mu_{FA}(s)$,whereas Subject 1 has the lowest. The lateral ADC heterogeneities of all subjects, $\mu_{ADC}(s)$, are almost coinciding, yet the LDC heterogeneities $\mu_{LDC}(s)$ differ again, with Subjects 2 and 1 having the largest and smallest lateral spreads, respectively. Table 4.2 depicts the numerical values of the Gaussian distribution parameters $\mu(s)$ and $\sigma(s)$ of the modeled indices. The base configuration diffusion anisotropy and SC plots indicate low inter subject variability in terms of the lateral heterogeneity of indices, whereas the Δ parameters show that the lateral heterogeneity of the change in diffusion anisotropy indices is the highest for Subject 1 and lowest for Subject 3. Figure 4.12 presents the inter subject variations of the Δ parameters.

All subjects have almost an identical lateral heterogeneity in terms of strain, which can be traced both numerically and visually from Table 4.2 and Figure 4.13. For all subjects the value of $\mu_{SC}(s)$ can be averaged from Table 4.2 as 0.0324 ± 0.0036, which indicates the small inter subject variability. Clearly, the strains imposed on the muscle fibers for all subjects are distributed heterogeneously on the lateral axes and this suggests the existence of heterogeneity in the lengthening or shortening of the sarcomeres arranged in parallel within the coinciding axial boundaries.

5.4. Longitudinal and Lateral Heterogeneity Assessment of LDC and Strain through Tractography Visuals

Figures 4.4 and 4.8 depict the spatial distribution of linear diffusion coefficients and strain coefficients, respectively, along the fiber tracts for all subjects. Figures 4.5 and 4.9 consist of the same population of fibers, with the colormaps indicating a single average parameter value for each fiber. Aside from the plots where all fibers are averaged longitudinally, the former couple of visuals depict the index distributions along individual fibers and therefore present a thorough analysis concerning the longitudinal heterogeneity. The latter two figures visualize the lateral spread of LDC and SC by assigning a distinct longitudinal average to each tract.

Figure 4.4a exemplifies that the diffusion of water molecules along the tract direction varies from the distal end to the proximal, as the majority of the fibers around the proximal end of the muscle have higher LDC, indicating a more facilitated diffusion at the specified locations. Toward the distal end, the general trend of the LDC index is decreasing, but there are portions with both higher and lower coefficients indicated with red green and red colors, respectively. It must be noted that the transitions between these regions are smooth and fiber bundles clustered around the same axial confounds seem to possess a more dramatic longitudinal heterogeneity compared to lateral. Increasing LDC values from the distal end to the proximal end are depicted in Figure 4.4b for Subject 2, similar to Subject 1. LDC distribution of Subject 3 follows the same trend as depicted in Figure 4.4c, including both longitudinal and lateral variations.

On Figure 4.8a the strain coefficient of Subject 1 is presented along fibers, where the global strain is around zero but small local variations exist, as is the case with Subject 3 on Figure

4.8c. Such local variations are more dominant in Figure 4.8b depicting the strain coefficient distribution of the second subject with a much higher number of fibers included (N = 1146). An important remark here is that both negative and positive local strains are present as the muscles move from flexed to extended configurations.

On figures 4.5 and 4.9, fiber averages are computed and used to generate colormaps for LDC and SC measures, respectively. These two figures indicate that on average, the diffusivity along tract direction as well as the distribution of strains are not locally similar for adjacent muscle fibers. When the heterogeneities within the distributions of strain along each fiber are averaged out, the remaining variations depicted in figures account for the heterogeneities in length changes of sarcomeres in parallel. These figures concur with the presence of intramuscular and epimuscular forces causing shear strains.

5.5. Remarks on the Deformation Analysis and Implications

Analysis through the tractography visuals (Figure 4.4, 4.5, 4.8 and 4.9) together with the longitudinal fiber average plots (Figure 4.1, 4.2, 4.3, 4.6), Gaussian probability distribution plots representing the longitudinal and lateral heterogeneity of the distribution of strain and diffusion parameters (Figures 4.10 through 4.13) and the values presented in Tables 4.1 and 4.2 imply that even though numerical indicators are not dramatically high, variations within the spatial distribution of strain and diffusion parameters along fibers and through axial slices exist as a result of the motion induced deformation.

The presence of lateral and longitudinal heterogeneity of strain is an indicator of myofascial force transmission. Although global strains can add up to zero, positive and negative local strains are distributed along fibers and within neighboring fiber bundles. When the muscles undergo passive extension from the flexed position, their relative positions with respect to surrounding tissues, bones, adjacent muscles as well as synergists and antagonists change. These alterations lead to the exertion of different loads from epimuscular and extramuscular connections. Because of such distinct loads applied at different locations of a target muscle, their distributions along the longitudinal and lateral directions are not homogeneous. Sarcomeres arranged in series along fibers and in parallel within fiber bundles therefore undergo heteroge-

neous length changes. Strain heterogeneity along the fiber direction can point to the presence of shear strains within the sarcomeres developed as a result of the change in muscle relative position.

Such shear strains also affect the diffusion along the fiber direction, as indicated from the changes of the fractional anisotropy, apparent diffusion coefficient and linear diffusion coefficient. Longitudinal and lateral analyses of the difference in diffusion parameter statistics (Δ parameters) as well as the individual distributions of indices along fibers show that heterogeneously distributed sarcomere lengths in series and in parallel affect diffusion in the tract direction, where the tract orientation is determined from the principal diffusion direction. The fact that the tracts are formed considering the principal diffusion directions explain the parallel trends of ADC and LDC indices.

The inter-subject analysis presented indicates a higher inter subject variability among diffusion anisotropy indices, whereas the strain coefficients of all patients are more similar. Figures 4.1 through 4.3 also depict that the parameter distributions within the fibers chosen for analysis do not follow the same trends; Subject 2 has an overall decreased LDC between the configurations, with the difference getting smaller from distal to the proximal end, whereas Subject 3 shows an opposite trend with an overall decreased LDC but increasing differences toward the proximal end. Inter-subject variability can be attributed to many factors, including height, weight and physiology. An example study was performed to investigate the gender effects [51], for instance, and it was found out that throughout seven calf muscles in 12 male and 12 female subjects, females had higher ADC and lower FA with respect to males. Our investigation here has only 3 female subjects so that the gender differences are opted out, and the subjects' ages, weights, heights and physical conditions were within a comparable range. A larger number of subjects would certainly contribute to the analysis. Variations between subjects could also be ascribed to the difference between the physical ranges of the acquired images along the leg and the number of fibers taken into consideration. Although the experimental protocols were the same in terms of the acquisition parameters, the datasets did not span identical volumes, possibly due to the varying leg lengths or patient positions. To minimize artifacts, regions of interests within which the fibers elongate were chosen to be as corresponding as possible. The number of fibers included in the analyses were comparable for

Subjects 2 and 3 whereas Subject 1 has a much lower fiber population. Though numerically different, the longitudinal and lateral heterogeneity indicators are comparable within their orders of magnitude.

Another constraint in the experiments are the dependence of the Δ parameters and the strain computations on the deformation field. The rigid and elastic registration steps to align the high resolution MR images between the two configuration were followed by the mapping of the high resolution field to the low resolution DT image. Any misalignment between the MR images could have caused deviations within calculations involving the displacement field.

Some other limitations of the results can be related to the data itself and the tractography algorithm. DT-MR images typically have low resolution and large artifacts, but for muscle images the signal-to-noise is even lower because muscles have low T2 compared to brain acquisitions [15]. Such noise in DT images can lead to early termination of fibers before reaching the aponeurosis, as could be the cause of the small number of fibers detected for Subject 1. It must be noted that four subjects were considered for the analysis, but one dataset failed to provide reliable number of fiber tracts with empirically reasonable orientations. In EPI-based techniques it is assumed that the spatial distortion arising from the magnetic inhomogeneities are negligible, as well as the movement artifacts in between acquisitions. Moreover fat suppression can be incomplete, causing chemical shift artifacts. Such artifacts were already present in the datasets, therefore non muscular regions were manually masked on the b0 images. More robust masks from high resolution MR images could ascertain the muscle boundaries, yet again an overall enhancement in DT-MRI acquisitions is more likely to ascertain accurate results.

For tractography, 4^{th} order Runge-Kutta integration based streamline algorithm described in [48] is preferred, where the seed inputs are chosen among the voxels with the maximum FA indices throughout the entire volume. Tracts are shaped through forward and backward iterations, merged after the stopping criterion is reached for each individual tract. Since muscle insertion and origins at specific locations are known, it is plausible to choose seed points from these locations and ensure tracts elongate from seed voxels to the muscle end. For the TA muscle, tracking from tibia or the superficial fascia to the central aponeurosis using masks obtained from anatomical images would also rule out the region of interest selection problem.

6. CONCLUSION

This thesis has presented a deformation analysis of skeletal muscles by assessing the spatial distributions of strain and diffusion characteristics along muscle fibers, using diffusion tensor magnetic resonance imaging. Diffusion anisotropy indices at the base and deformed configurations of the TA muscle of lower leg were analyzed as well as the local and global strain measures along muscle fiber directions. Longitudinal and lateral heterogeneities within the distributions of individual parameters were modeled and presented to account for the biomechanical changes of the muscle microstructure as a result of the deformation caused by the position change of the leg.

The methodology presented here has provided an image processing toolbox for the analysis of skeletal muscle fiber architecture. Experimental results have revealed the spatial distribution of diffusion anisotropy in terms of FA, ADC and LDC indices along the fibers in base configuration. Proximo-distal diffusion anisotropy differences were detected as well as heterogeneities on the transverse slices for the flexed position of the lower leg.

The change of the diffusion anisotropy indices along fibers as the leg is extended is found to possess local heterogeneities along each fiber and on the transverse slices, which is also the case for the spatial distribution of strain along fiber direction. For the three subjects considered, local fluctuations of the imposed global strain were detected.

Longitudinal and lateral heterogeneities of the change in the linear diffusion coefficient and local strains computed along the fiber direction point to the existence of shear strains and epimuscular myofascial force transmission, because as the muscle relative position changes due to movement, unequal loads are imposed from different sections of the muscle, thereby affecting sarcomere length changes at distinct proximities in a heterogeneous fashion.

This thesis provides a unique framework in the sense that it investigates the deformation and thereby the microstructure of skeletal muscles in terms of the diffusion anisotropy changes and strains along muscle fiber directions rather than outside coordinate systems. Because no golden standards exist for the analysis of the results, empirical evaluations were presented with colormap visuals of the measured parameters, parameter averages over all fibers were longitudinally and laterally modeled as numerical indicators and for inter-subject comparisons.

Future work for the investigation involves the comparison of strain tensor and diffusion tensor eigenanalyses along fibers, which would provide further insight into the correlations between the local fiber orientation changes and length changes. Analyses of synergistic and antagonistic muscles together would also strengthen the demonstration of epimuscular myofascial force transmission. Diffusion based analyses can be improved by including the examination of diffusion coefficients along the directions orthogonal to the tract orientation. Discovering the physical correlates of the second and third eigenvalues of the diffusion tensor can improve the assessment of microstructural changes occuring as a result of any deformation.

APPENDIX A: PARAMETER PLOTS ALONG INDIVIDUAL FIBERS

In this appendix, individual fiber statistics of all parameters are plotted confined to the confidence range of each subject. Number of fibers included in the analyses are 167, 1146 and 1006 for subjects 1, 2 and 3, respectively.

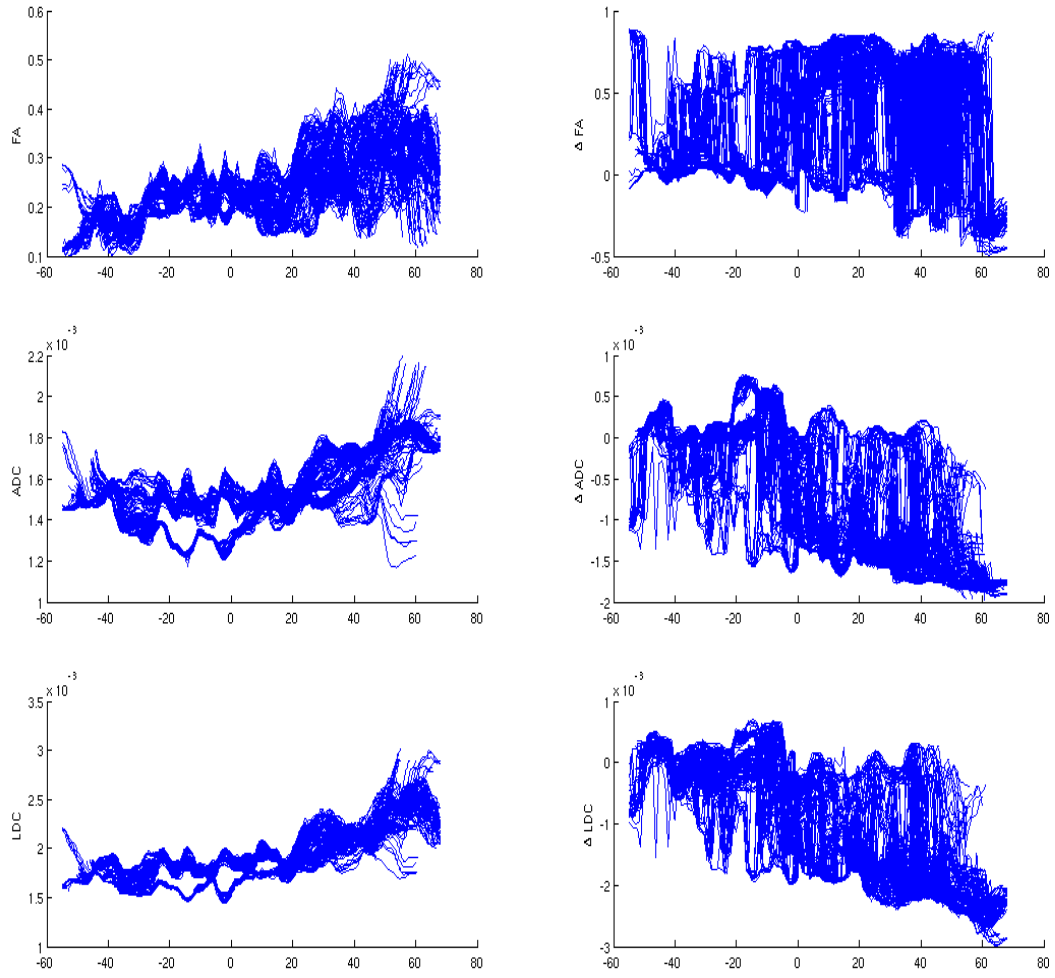

Figure A.1. FA, ADC, LDC (right column, top to bottom) and ΔFA, ΔADC, ΔLDC (left column, top to bottom) along fiber tracts of Subject 1, within the subject's confidence range.

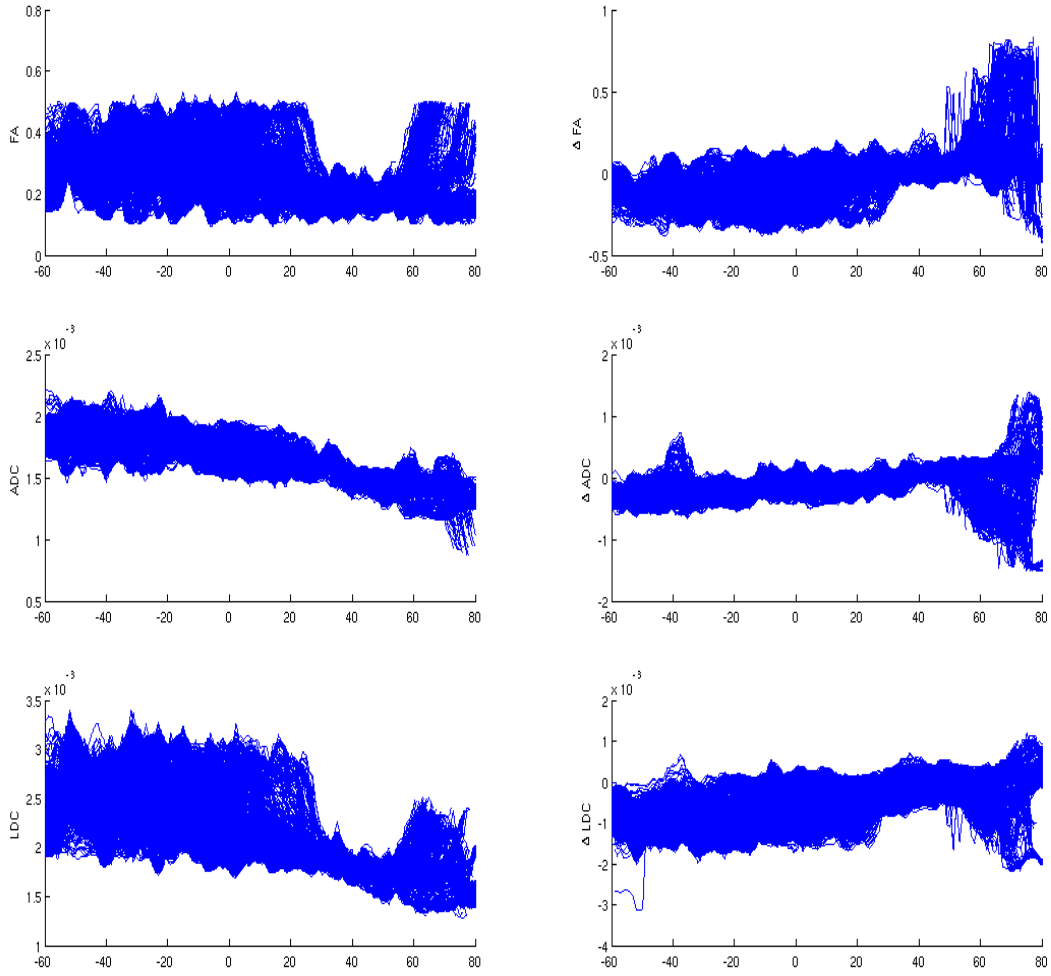

Figure A.2. FA, ADC, LDC (right column, top to bottom) and ΔFA, ΔADC, ΔLDC (left column, top to bottom) along fiber tracts of Subject 2, within the subject's confidence range.

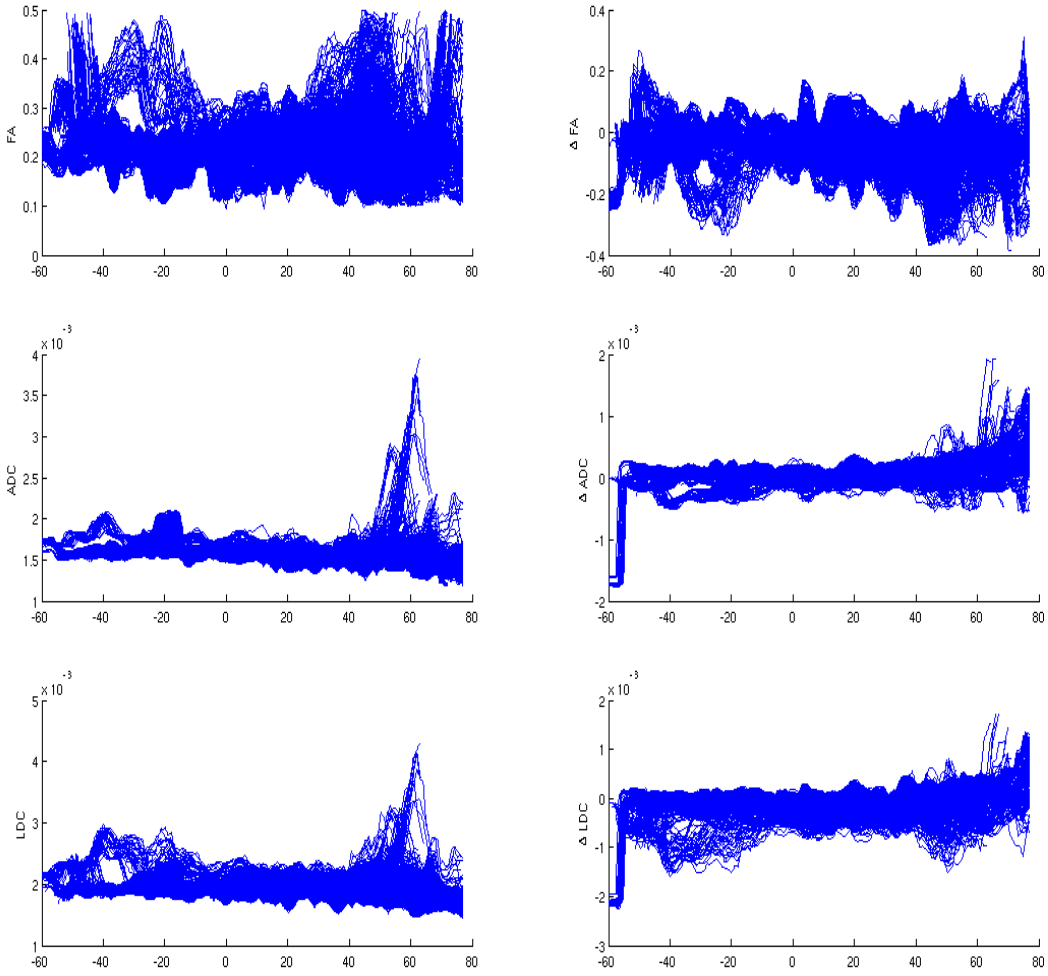

Figure A.3. FA, ADC, LDC (right column, top to bottom) and ΔFA, ΔADC, ΔLDC (left column, top to bottom) along fiber tracts of Subject 3, within the subject's confidence range.

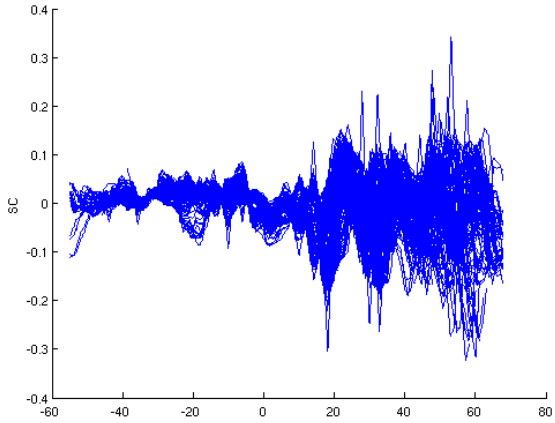

(a) Subject 1

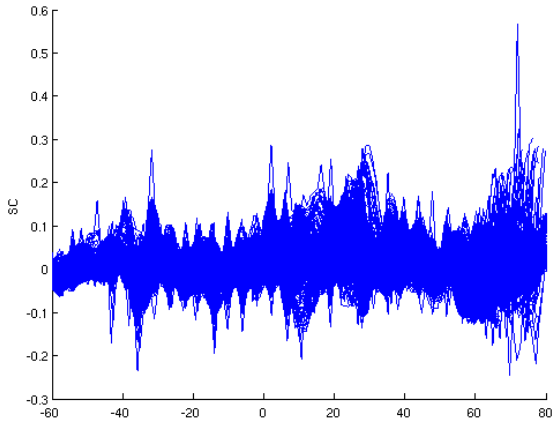

(b) Subject 2

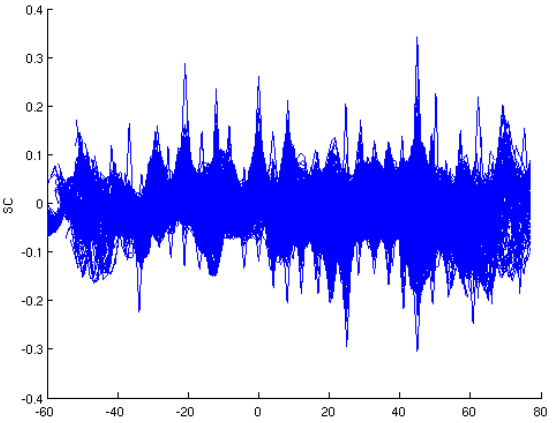

(c) Subject 3

Figure A.4. SC along all fiber tracts of Subjects 3, 4 and 5 from top to bottom, respectively, within the confidence ranges of each subject.

REFERENCES

1. Yucesoy, C. A., "Epimuscular Myofascial Force Transmission Implies Novel Principles for Muscular Mechanics", *Exercise and Sport Sciences Reviews*, Vol. 38, No. 3, pp. 128–134, 2010.

2. Huijing, P. A., "Muscle as a Collagen Fiber Reinforced Composite: a Review of Force Transmission in Muscle and Whole Limb", *Journal of Biomechanics*, Vol. 32, No. 4, pp. 329–345, 1999.

3. Street, S. F., "Lateral Transmission of Tension in Frog Myofibers: a Myofibrillar Network and Transverse Cytoskeletal Connections are Possible Transmitters", *Journal of Cellular Physiology*, Vol. 114, No. 3, pp. 346–364, 1983.

4. Yucesoy, C. A., B. H. Koopman, P. A. Huijing and H. J. Grootenboer, "Three-Dimensional Finite Element Modeling of Skeletal Muscle using a Two-Domain Approach: Linked Fiber-Matrix Mesh Model", *Journal of Biomechanics*, Vol. 35, No. 9, pp. 1253–1262, 2002.

5. Yucesoy, C. A., G. C. Baan, B. H. Koopman, H. J. Grootenboer and P. A. Huijing, "Pre-Strained Epimuscular Connections Cause Muscular Myofascial Force Transmission to Affect Properties of Synergistic EHL and EDL Muscles of the Rat", *Journal of Biomechanical Engineering*, Vol. 127, No. 5, pp. 819–828, 2005.

6. Huijing, P. A., "Epimuscular Myofascial Force Transmission Between Antagonistic and Synergistic Muscles Can Explain Movement Limitation in Spastic Paresis", *Journal of Electromyography and Kinesiology*, Vol. 17, No. 6, pp. 708–724, 2007.

7. Huijing, P. A., A. Yaman, C. Ozturk and C. A. Yucesoy, "Effects of Knee Joint Angle on Global and Local Strains within Human Triceps Surae Muscle: MRI Analysis Indicating In Vivo Myofascial Force Transmission Between Synergistic Muscles", *Surgical and Radiologic Anatomy*, Vol. 33, No. 10, pp. 869–879, 2011.

8. Yaman, A., C. Ozturk, P. Huijing and C. Yucesoy, "Magnetic Resonance Imaging Assessment of Mechanical Interactions Between Human Lower Leg Muscles in Vivo", *Journal of Biomechanical Engineering*, Vol. 135, No. 9, pp. 091003–1–091003–9, 2013.

9. Yucesoy, C. A. and P. A. Huijing, "Substantial Effects of Epimuscular Myofascial Force Transmission on Muscular Mechanics Have Major Implications on Spastic Muscle and Remedial Surgery", *Journal of Electromyography and Kinesiology*, Vol. 17, No. 6, pp. 664–679, 2007.

10. Yucesoy, C. A., B. H. Koopman, H. J. Grootenboer and P. A. Huijing, "Finite Element Modeling of Aponeurotomy: Altered Intramuscular Myofascial Force Transmission Yields Complex Sarcomere Length Distributions Determining Acute Effects", *Biomechanics and Modeling in Mechanobiology*, Vol. 6, No. 4, pp. 227–243, 2007.

11. Yucesoy, C. A., B. H. Koopman, H. J. Grootenboer and P. A. Huijing, "Extramuscular Myofascial Force Transmission Alters Substantially the Acute Effects of Surgical Aponeurotomy: Assessment by Finite Element Modeling", *Biomechanics and Modeling in Mechanobiology*, Vol. 7, No. 3, pp. 175–189, 2008.

12. Yucesoy, C. A. and P. A. Huijing, "Assessment by Finite Element Modeling Indicates that Surgical Intramuscular Aponeurotomy Performed Closer to the Tendon Enhances Intended Acute Effects in Extramuscularly Connected Muscle", *Journal of Biomechanical Engineering*, Vol. 131, No. 2, 2009.

13. Ateş, F., Y. Temelli and C. A. Yucesoy, "Human Spastic Gracilis Muscle Isometric Forces Measured Intraoperatively as a Function of Knee Angle Show No Abnormal Muscular Mechanics", *Clinical Biomechanics*, 2012.

14. Heemskerk, A. M., T. K. Sinha, K. J. Wilson, Z. Ding and B. M. Damon, "Repeatability of DTI-Based Skeletal Muscle Fiber Tracking", *NMR in Biomedicine*, Vol. 23, No. 3, pp. 294–303, 2010.

15. Sinha, S., U. Sinha and V. R. Edgerton, "In Vivo Diffusion Tensor Imaging of the Human

Calf Muscle", *Journal of Magnetic Resonance Imaging*, Vol. 24, No. 1, pp. 182–190, 2006.

16. Schwenzer, N. F., G. Steidle, P. Martirosian, C. Schraml, F. Springer, C. D. Claussen and F. Schick, "Diffusion Tensor Imaging of the Human Calf Muscle: Distinct Changes in Fractional Anisotropy and Mean Diffusion due to Passive Muscle Shortening and Stretching", *NMR in Biomedicine*, Vol. 22, No. 10, pp. 1047–1053, 2009.

17. Kingsley, P. B., "Introduction to Diffusion Tensor Imaging Mathematics: Part II. Anisotropy, Diffusion-Weighting Factors, and Gradient Encoding Schemes", *Concepts in Magnetic Resonance Part A*, Vol. 28, No. 2, pp. 123–154, 2006.

18. Damon, B. M., Z. Ding, A. W. Anderson, A. S. Freyer and J. C. Gore, "Validation of Diffusion Tensor MRI-Based Muscle Fiber Tracking", *Magnetic Resonance in Medicine*, Vol. 48, No. 1, pp. 97–104, 2002.

19. Bammer, R., B. Acar and M. E. Moseley, "In Vivo MR Tractography using Diffusion Imaging", *European Journal of Radiology*, Vol. 45, No. 3, pp. 223–234, 2003.

20. Heemskerk, A. M., T. K. Sinha, K. J. Wilson, Z. Ding and B. M. Damon, "Quantitative Assessment of DTI-Based Muscle Fiber Tracking and Optimal Tracking Parameters", *Magnetic Resonance in Medicine*, Vol. 61, No. 2, pp. 467–472, 2009.

21. Basser, P. J., J. Mattiello and D. LeBihan, "MR Diffusion Tensor Spectroscopy and Imaging", *Biophysical Journal*, Vol. 66, No. 1, pp. 259–267, 1994.

22. Basser, P. J., "Inferring Microstructural Features and the Physiological State of Tissues from Diffusion-Weighted Images", *NMR in Biomedicine*, Vol. 8, No. 7, pp. 333–344, 1995.

23. Le Bihan, D., J.-F. Mangin, C. Poupon, C. A. Clark, S. Pappata, N. Molko and H. Chabriat, "Diffusion Tensor Imaging: Concepts and Applications", *Journal of Magnetic Resonance Imaging*, Vol. 13, No. 4, pp. 534–546, 2001.

24. Yang, F., Y.-M. Zhu, I. E. Magnin, J.-H. Luo, P. Croisille and P. B. Kingsley, "Feature-

Based Interpolation of Diffusion Tensor Fields and Application to Human Cardiac DT-MRI", *Medical Image Analysis*, Vol. 16, No. 2, pp. 459–481, 2012.

25. Cleveland, G., D. Chang, C. Hazlewood and H. Rorschach, "Nuclear Magnetic Resonance Measurement of Skeletal Muscle: Anisotrophy of the Diffusion Coefficient of the Intracellular Water", *Biophysical Journal*, Vol. 16, No. 9, pp. 1043–1053, 1976.

26. Dougherty, G., "Image Analysis in Medical Imaging: Recent Advances in Selected Examples", *Biomedical Imaging and Intervention Journal*, Vol. 6, No. 3, p. e32, 2010.

27. Hagmann, P., L. Jonasson, P. Maeder, J.-P. Thiran, V. J. Wedeen and R. Meuli, "Understanding Diffusion MR Imaging Techniques: From Scalar Diffusion-weighted Imaging to Diffusion Tensor Imaging and Beyond1", *Radiographics*, Vol. 26, No. suppl 1, pp. S205–S223, 2006.

28. Zaraiskaya, T., D. Kumbhare and M. D. Noseworthy, "Diffusion Tensor Imaging in Evaluation of Human Skeletal Muscle Injury", *Journal of Magnetic Resonance Imaging*, Vol. 24, No. 2, pp. 402–408, 2006.

29. Basser, P. J., S. Pajevic, C. Pierpaoli, J. Duda and A. Aldroubi, "In Vivo Fiber Tractography using DT-MRI Data", *Magnetic Resonance in Medicine*, Vol. 44, No. 4, pp. 625–632, 2000.

30. Turner, R. and D. Le Bihan, "Single-Shot Diffusion Imaging at 2.0 Tesla", *Journal of Magnetic Resonance (1969)*, Vol. 86, No. 3, pp. 445–452, 1990.

31. Jezzard, P., A. S. Barnett and C. Pierpaoli, "Characterization of and Correction for Eddy Current Artifacts in Echo Planar Diffusion Imaging", *Magnetic Resonance in Medicine*, Vol. 39, No. 5, pp. 801–812, 1998.

32. Heemskerk, A. M. and B. M. Damon, "Diffusion Tensor MRI Assessment of Skeletal Muscle Architecture", *Current Medical Imaging Reviews*, Vol. 3, No. 3, pp. 152–160, 2007.

33. Van Donkelaar, C., L. Kretzers, P. Bovendeerd, L. Lataster, K. Nicolay, J. Janssen and M. Drost, "Diffusion Tensor Imaging in Biomechanical Studies of Skeletal Muscle Function", *Journal of Anatomy*, Vol. 194, No. 1, pp. 79–88, 1999.

34. Tseng, W.-Y. I., V. J. Wedeen, T. G. Reese, R. N. Smith and E. F. Halpern, "Diffusion Tensor MRI of Myocardial Fibers and Sheets: Correspondence with Visible Cut-Face Texture", *Journal of Magnetic Resonance Imaging*, Vol. 17, No. 1, pp. 31–42, 2003.

35. Galban, C. J., S. Maderwald, K. Uffmann, A. de Greiff and M. E. Ladd, "Diffusive Sensitivity to Muscle Architecture: a Magnetic Resonance Diffusion Tensor Imaging Study of the Human Calf", *European Journal of Applied Physiology*, Vol. 93, No. 3, pp. 253–262, 2004.

36. Powell, P. L., R. R. Roy, P. Kanim, M. A. Bello and V. R. Edgerton, "Predictability of Skeletal Muscle Tension from Architectural Determinations in Guinea Pig Hindlimbs", *Journal of Applied Physiology*, Vol. 57, No. 6, pp. 1715–1721, 1984.

37. Heemskerk, A. M., M. R. Drost, G. S. van Bochove, M. F. van Oosterhout, K. Nicolay and G. J. Strijkers, "DTI-Based Assessment of Ischemia-Reperfusion in Mouse Skeletal Muscle", *Magnetic Resonance in Medicine*, Vol. 56, No. 2, pp. 272–281, 2006.

38. Saotome, T., M. Sekino, F. Eto and S. Ueno, "Evaluation of Diffusional Anisotropy and Microscopic Structure in Skeletal Muscles using Magnetic Resonance", *Magnetic Resonance Imaging*, Vol. 24, No. 1, pp. 19–25, 2006.

39. Budzik, J.-F., V. Le Thuc, X. Demondion, M. Morel, D. Chechin and A. Cotten, "In Vivo MR Tractography of Thigh Muscles using Diffusion Imaging: Initial Results", *European Radiology*, Vol. 17, No. 12, pp. 3079–3085, 2007.

40. Heemskerk, A., T. Sinha, Z. Ding, C. Blyth and B. Damon, "Reproducibility of DTI-Based Muscle Fiber Tracking", *Proceedings of the 16th Scientific meeting ISMRM*, 2007.

41. Englund, E. K., C. P. Elder, Q. Xu, Z. Ding and B. M. Damon, "Combined Diffusion and

Strain Tensor MRI Reveals a Heterogeneous, Planar Pattern of Strain Development During Isometric Muscle Contraction", *American Journal of Physiology-Regulatory, Integrative and Comparative Physiology*, Vol. 300, No. 5, pp. R1079–R1090, 2011.

42. Hiblar, T., E. Bolson, M. Hubka, F. Sheehan and M. Kushmerick, "Three Dimensional Ultrasound Analysis of Fascicle Orientation in Human Tibialis Anterior Muscle Enables Analysis of Macroscopic Torque at the Cellular Level", *Molecular and Cellular Aspects of Muscle Contraction*, pp. 635–645, Springer, 2003.

43. Lansdown, D. A., Z. Ding, M. Wadington, J. L. Hornberger and B. M. Damon, "Quantitative Diffusion Tensor MRI-Based Fiber Tracking of Human Skeletal Muscle", *Journal of Applied Physiology*, Vol. 103, No. 2, pp. 673–681, 2007.

44. Blemker, S. S., P. M. Pinsky and S. L. Delp, "A 3D Model of Muscle Reveals the Causes of Nonuniform Strains in the Biceps Brachii", *Journal of Biomechanics*, Vol. 38, No. 4, pp. 657–665, 2005.

45. "Review of Continuum Mechanics", `http://www.colorado.edu/engineering/cas/courses.d/NFEM.d/NFEM.Ch07.d/NFEM.Ch07.pdf`, accessed at August, 2013.

46. Thirion, J.-P., "Image Matching as a Diffusion Process: An Analogy with Maxwell's Demons", *Medical Image Analysis*, Vol. 2, No. 3, pp. 243–260, 1998.

47. Lubliner, J., *Plasticity Theory*, Courier Dover Publications, New York, 2008.

48. Tench, C., P. Morgan, M. Wilson and L. Blumhardt, "White Matter Mapping using Diffusion Tensor MRI", *Magnetic Resonance in Medicine*, Vol. 47, No. 5, pp. 967–972, 2002.

49. "NIH Blueprint: The Human Connectome Project", `http://www.humanconnectome.org/about/project/tractography.html`, accessed at August, 2013.

50. Arsigny, V., P. Fillard, X. Pennec and N. Ayache, "Log-Euclidean Metrics for Fast and Simple Calculus on Diffusion Tensors", *Magnetic Resonance in Medicine*, Vol. 56, No. 2,

pp. 411–421, 2006.

51. Galban, C. J., S. Maderwald, K. Uffmann and M. E. Ladd, "A Diffusion Tensor Imaging Analysis of Gender Differences in Water Diffusivity within Human Skeletal Muscle", *NMR in Biomedicine*, Vol. 18, No. 8, pp. 489–498, 2005.